have an important interaction so that d_{xz} is more delocalized on the ligands than d_{xy} and has a smaller overlap with π^*_{CO} of R_2CO. Secondly the ligand-ligand 4e repulsive interactions are stronger for PH_3 than for Cl.

Finally, in $CpM(CO)_2(\eta_2\text{-}R_2CO)$ complexes, the C=O bond bisects the molecular mirror plane as in ethylene complexes.[23] The CO's must be bent back by 10° in order to remove the steric hindrance between C and the CO ligand (C-C overlap population of 0.08). For the $CpRe^+(NO)PH_3(R_2CO)$ complexes, the experimental geometry has been taken both in the η_1[13] and η_2[14a] forms. The orientation of R_2CO is such that the π^*_{CO} orbital overlaps with the HOMO of the metallic part (see Scheme II).

Photosynthetic Water Oxidation Center: Spin Frustration in Distorted Cubane $Mn^{IV}Mn^{III}_3$ Model Complexes

David N. Hendrickson,*[1a] George Christou,*[2a] Edward A. Schmitt,[1a] Eduardo Libby,[2a] John S. Bashkin,[2a] Sheyi Wang,[2a] Hui-Lien Tsai,[1a] John B. Vincent,[2a] Peter D. W. Boyd,[3] John C. Huffman,[2b] Kirsten Folting,[2b] Qiaoying Li,[1b] and William E. Streib[2b]

Contribution from the Department of Chemistry-0506, University of California at San Diego, La Jolla, California 92093-0506, and the Department of Chemistry and the Molecular Structure Center, Indiana University, Bloomington, Indiana 47405. *Received August 14, 1991*

Abstract: Four $Mn^{IV}Mn_3^{III}$ complexes have been prepared as model complexes for the S_2 state of the water oxidation center (WOC) in photosystem II. All of these complexes are prepared by the reaction of a μ_3-oxide Mn_3^{III} complex with Me_3SiCl which leads to a disproportionation to give the $Mn^{IV}Mn_3^{III}$ complex and an Mn^{II} product. The reaction of $Mn(O_2CCH_3)_3\cdot 2H_2O$ with Me_3SiCl followed by addition of imidazole gives $(H_2Im)_2[Mn_4O_3Cl_6(O_2CCH_3)_3(HIm)]\cdot{}^3/_2CH_3CN$ (**1**) where H_2Im^+ is the imidazolium cation. Reaction of $[Mn_3O(O_2CCH_3)_6(py)_3](ClO_4)$ or $[Mn_3O(O_2CCH_2CH_3)_6(py)_3](ClO_4)$ with Me_3SiCl leads, respectively, to $[Mn_4O_3Cl_4(O_2CCH_3)_3(py)_3]\cdot{}^3/_2CH_3CN$ (**2**) and $[Mn_4O_3Cl_4(O_2CCH_2CH_3)_3(py)_3]\cdot{}^5/_2CH_3CN$ (**4**). A similar procedure as for **2** but followed by addition of imidazole yields $[Mn_4O_3Cl_4(O_2CCH_3)_3(HIm)_3]\cdot{}^5/_2CH_3CN$ (**5**). Complex **1** crystallizes in the orthorhombic space group *Pbca* with (at −158 °C) a = 14.307 (14) Å, b = 14.668 (14) Å, c = 31.319 (36) Å, V = 6572.75 Å^3, and Z = 8. A total of 2513 unique data with $F > 2.33\sigma(F)$ were refined to values of R and R_w of 8.10 and 8.70%, respectively. The central $[Mn_4(\mu_3\text{-}O)_3(\mu_3\text{-}Cl)]^{6+}$ core of the anion in complex **1** consists of a Mn_4 pyramid with the Mn^{IV} ion at the apex, a μ_3-Cl^- ion bridging the basal plane, and a μ_3-O^{2-} ion bridging each of the remaining three faces. The Mn^{IV} ion has six oxygen atom ligands, three from the three μ_3-O^{2-} ions and three from the bridging acetates. Two of the Mn^{III} ions have $Mn(Cl)_2(\mu_3\text{-}Cl)(\mu_3\text{-}O)_2(\mu\text{-}O_2CCH_3)$ coordination spheres; the third Mn^{III} ion has one of the terminal Cl^- ligands replaced by an imidazole ligand. The complex $[Mn_4O_3Cl_4(O_2CCH_3)_3(py)_3]\cdot{}^3/_2CH_3CN$ (**2**) crystallizes in the hexagonal space group $R\bar{3}$ with (at −155 °C) $a = b = c$ = 13.031 (4) Å, $\alpha = \beta = \gamma$ = 74.81 (2)°, V = 2015.93 Å^3, and Z = 2. A total of 1458 unique data with $F > 3.0\sigma(F)$ were refined to values of R and R_w of 3.71 and 4.17%, respectively. The $Mn^{IV}Mn_3^{III}O_3Cl$ core in complex **2** is essentially superimposable with that of complex **1**. Complex **2** has crystallographically imposed C_3 symmetry. The other two complexes, $[Mn_4O_3Cl_4(O_2CCH_2CH_3)_3(py)_3]\cdot{}^5/_2CH_3CN$ (**4**) and $[Mn_4O_3Cl_4(O_2CCH_3)_3(HIm)_3]\cdot{}^5/_2CH_3CN$ (**5**), also crystallize in the $R\bar{3}$ space group. The unit cell of complex **4** has (at −143 °C) $a = b = c$ = 13.156 (6) Å, $\alpha = \beta = \gamma$ = 74.56 (3)°, V = 2068.53 Å^3, and Z = 2. A total of 1425 unique data with $F > 3.0\sigma(F)$ were refined to values of R and R_w of 5.265 and 5.44%, respectively. The unit cell of complex **5** has (at −145 °C) $a = b$ = 15.656 (6) Å, c = 26.947 (9) Å, $\alpha = \beta$ = 90°, γ = 120.0°, V = 5722.68 Å^3, and Z = 6. A total of 1156 unique data with $F > 3.0\sigma(F)$ was refined to values of R and R_w of 5.75 and 5.90%, respectively. The $Mn^{IV}Mn_3^{III}O_3Cl$ core of these complexes is compared with the core of S_1-state model complexes which have the $Mn_4^{III}(\mu_3\text{-}O)_2$ butterfly structure. It is suggested that increasing the oxidation state from S_1 to S_2 state is coupled to an increase in oxide content. A strong Mn-O stretching IR band at 580-590 cm^{-1} is identified as characteristic of $Mn^{IV}Mn_3^{III}O_3Cl$ cubane complexes. No reversible waves were observed in the electrochemistry of these complexes. However, ^{1}H NMR and Beers law dependence studies show that complex **1** remains intact in DMF as do complexes **2** and **4** in CH_2Cl_2 and $CHCl_3$. Magnetic susceptibility data are presented for complexes **1**, **2**, and **4** at 10.0 kG in the 5-300 K range. The value of μ_{eff}/molecule at room temperature increases with decreasing temperature to give a maximum at 60 K for **1** and **2** and 15 K for **4**. Below these temperatures μ_{eff}/molecule drops relatively abruptly. The data were fit to a theoretical model to give exchange parameters $J_{34}(Mn^{IV}\cdots Mn^{III})$ of −20.8 to −30.3 cm^{-1} and J_{33} of +8.6 to 11.3 cm^{-1}. The ground state for all complexes is a well-isolated $S_T = {}^9/_2$ state. This was confirmed by variable field magnetization studies: ~2-40 K at fields of 24.8, 34.5, and 44.0 kG for complex **2**; ~2-15 K at fields of 10.0, 30.0, and 48.0 kG for complex **4**. These data were fit by a matrix diagonalization approach with Zeeman and axial zero-field ($D\hat{S}_z^2$) interactions to verify a $S_T = {}^9/_2$ ground state with $D \simeq +0.3$ cm^{-1}. The nature of the spin frustration in these $Mn^{IV}Mn_3^{III}O_3Cl$ cubane complexes is analyzed in detail. It is shown what other ground states may be possible for such a complex. Variable-temperature X-band EPR data are presented for polycrystalline and frozen glass samples of complexes **1**, **2**, and **4**. Q-band spectra are also given for solid samples. A detailed map of expected X-band resonance fields plotted versus the axial zero-field splitting parameter is derived for a complex with $S_T = {}^9/_2$ ground state. The experimental EPR spectra are shown to be qualitatively in agreement with these calculated resonance fields. The electronic structure of the four $Mn^{IV}Mn_3^{III}O_3Cl$ cubane complexes is discussed with the goal of modeling the S_2 state of the WOC.

Introduction

Polynuclear metal complexes are found as the active sites in several metalloproteins. The electronic structures of many of these polynuclear active sites are complicated, and, as a consequence, there is a sensitivity to extrinsic factors. Recent work[4,5] on $[Fe_4S_4(SR)_4]^{3-}$ complexes which mimic the active sites in certain electron transport proteins has established that these complexes

(1) (a) University of California at San Diego. (b) Present address: University of California at Santa Barbara.
(2) (a) Department of Chemistry, Indiana University. (b) Molecular Structure Center, Indiana University.
(3) On sabbatical leave from the University of Auckland, Auckland, New Zealand.

(4) Carney, M. J.; Papaefthymiou, G. C.; Spartalian, K.; Frankel, R. B.; Holm, R. H. *J. Am. Chem. Soc.* **1988**, *110*, 6084-6095, and references therein.
(5) Carney, M. J.; Papaefthymiou, G. C.; Whitener, M. A.; Spartalian, K.; Frankel, R. B.; Holm, R. H. *Inorg. Chem.* **1988**, *27*, 346-352.

0002-7863/92/1514-2455$03.00/0 © 1992 American Chemical Society

show a structural and spin-state variability. In addition to $S = {}^1/_2$ and $S = {}^3/_2$ ground states, the $[Fe_4S_4(SR)_4]^{3-}$ complexes exhibit ground states characterized as either physical mixtures of $S = {}^1/_2$ and $S = {}^3/_2$ species or as a spin-admixed species. It is of interest to note that proteins and enzymes with this $[Fe_4S_4(SR)_4]^{3-}$ active site have also been reported[6] to have either $S = {}^1/_2, {}^3/_2, {}^5/_2$ or even larger spin ground states. For the model complexes there is not a simple correlation between the room-temperature X-ray structural details and the spin of the ground state. In fact, exactly which ground state is present is dependent on the environment about the $[Fe_4S_4(SR)_4]^{3-}$ complex. Changes in ground states of $[Fe_4S_4(SR)_4]^{3-}$ from a polycrystalline state to a frozen glass medium and the observation of physical mixtures of different spin state species is quite reminiscent of the behavior of spin-crossover complexes.[7] These mononuclear complexes (many Fe^{II} and Fe^{III}) change not only from one spin state to another with changes in temperature but also with subtle environmental changes such as the presence of a solvate molecule in the crystal or even mild grinding of a polycrystalline sample.[8] There are only two cluster complexes which have been established to show the spin-crossover phenomenon. In the solid state Nb_6I_{11} converts from a $S = {}^1/_2$ to a $S = {}^3/_2$ ground state as the temperature is increased, and HNb_6H_{11} converts from a $S = 0$ to a $S = 1$ ground state.[9] The sensitivities of the ground state of the above iron and niobium complexes is likely a manifestation of the vibronic nature[10] of these complexes. Such a pronounced sensitivity of electronic structure to environmental factors is well-known for other vibronically active species such as mixed-valence complexes.[11]

Even though there is discussion about the exact topological arrangement, it is clear that four manganese ions are involved in the water oxidation center (WOC) of photosystem II.[12] This Mn_4 site is oxidized one electron at a time and cycles among five states (oxidation states) during water oxidation. The Kok[13] states are designated as S_0, S_1, S_2, S_3, and S_4. Only in the $S_4 \rightarrow S_0$ step is water oxidized to give oxygen. The S_2 state is believed to have a $Mn^{IV}Mn_3^{III}$ active site. An analysis of the multiline (16 or more features) EPR signal centered in the $g = 2$ region clearly establishes that two and more likely four manganese ions are exchange coupled in the S_2 state.[14] The characteristics of this multiline EPR signal have been taken to indicate that this Mn_4 S_2-state species has a $S = {}^1/_2$ ground state. A second S_2-state EPR signal occurs in the $g = 4.1$ region.[15] The temperature dependencies[16,17] of the two different EPR signals and observations[18,19] of the interconversion between the multiline $g = 2$ and the $g = 4.1$ signals have led to two different theories for the origins of the two S_2-state EPR signals. Brudvig et al.[16,19,20] concluded that the two EPR signals arise from two different conformations of a single tetranuclear manganese site. On the other hand, Hansson et al.[17] suggested that the $g = 4.1$ signal comes from an isolated Mn^{IV} ion which is in a redox-equilibrium with a trinuclear manganese site that gives rise to the multiline $g = 2$ signal. However, Kim et al.[21] showed that this latter interpretation is not correct. With oriented PSII membranes under conditions of ammonia inhibition of O_2 evolution they found that the $g = 4.1$ signal exhibits at least 16 manganese hyperfine lines. The $g = 4.1$ signal clearly comes from a polynuclear manganese site and exhibits strain effects as have reported[22] for the EPR spectra of $Mn^{II}Mn^{III}$ binuclear complexes. Thus, it appears that depending on conditions the $Mn^{IV}Mn_3^{III}$ site can have either a $S = {}^1/_2$ or a $S = {}^3/_2$ ground state.

Only three tetranuclear manganese complexes modeling the S_2-state $Mn^{IV}Mn_3^{III}$ oxygen evolving complex have been reported: $(H_2Im)_2[Mn_4O_3Cl_6(O_2CCH_3)_3(HIm)]\cdot{}^3/_2CH_3CN$ (**1**, H_2Im^+ = imidazolium cation),[23] $[Mn_4O_3Cl_4(O_2CCH_3)_3(py)_3]\cdot{}^3/_2CH_3CN$ (**2**, py = pyridine),[24] and $[Mn_4O_3Cl(O_2CCH_3)_3(dbm)_3]$ (**3**, dbmH = dibenzoylmethane).[25] For complex **3** the conversion from an

(6) (a) Huynh, B. H.; Henzl, M. T.; Christner, J. A.; Zimmerman, R.; Orme-Johnson, W. H.; Münck, E. *Biochim. Biophys. Acta* **1980**, *623*, 124. (b) Johnson, M. K.; Thomson, A. J.; Robinson, A. E.; Smith, B. E. *Biochim. Biophys. Acta* **1981**, *671*, 61. (c) Smith, J. P.; Emptage, M. H.; Orme-Johnson, W. H. *J. Biol. Chem.* **1982**, *257*, 2310. (d) Moringstar, J. E.; Johnson, M. K.; Case, E. E.; Hales, B. J. *Biochemistry* **1987**, *26*, 1795. (e) Vollmer, S. J.; Switzer, R. L.; Debrunner, P. G. *J. Biol. Chem.* **1983**, *258*, 14284. (f) Rusnak, F. M.; Adams, M. W. W.; Mortenson, L. E.; Münck, E. *J. Biol. Chem.* **1987**, *262*, 38. (g) Morgan, T. V.; Prince, R. C.; Mortenson, L. E. *FEBS Lett.* **1986**, *206*, 4. (h) Hagen, W. R.; Wassink, H.; Eady, R. R.; Smith, B. E.; Haaker, H. *Eur. J. Biochem.* **1987**, *169*, 457. (i) McLean, P. A.; Papaefthymiou, V.; Orme-Johnson, W. H.; Münck, E. *J. Biol. Chem.* **1987**, *262*, 12900. (j) Bertrand, P.; Gayda, J.-P.; Rao, K. K. *J. Chem. Phys.* **1982**, *76*, 4715. (k) Middleton, P.; Dickson, D. P. E.; Johnson, C. E.; Rush, J. D. *Eur. J. Biochem.* **1978**, *88*, 135. (l) Christner, J. A.; Münck, E.; Janik, P. A.; Siegel, L. M. *J. Biol. Chem.* **1981**, *256*, 2098. (m) Auric, P.; Gaillard, J.; Meyer, J.; Moulis, J.-M. *Biochem. J.* **1987**, *242*, 525. (n) Lindahl, P. A.; Day, E. P.; Kent, T. A.; Orme-Johnson, W. H.; Münck, E. *J. Biol. Chem.* **1985**, *260*, 11160. (o) Lindahl, P. A.; Gorelick, N. J.; Münck, E.; Orme-Johnson, W. H. *J. Biol. Chem.* **1987**, *262*, 14945.

(7) (a) Beattie, J. K. *Adv. Inorg. Chem.* **1988**, *32*, 1–53. (b) König, E. *Prog. Inorg. Chem.* **1987**, *35*, 527–622. (c) Rao, C. N. R. *Int. Rev. Phys. Chem.* **1985**, *4*, 19. (d) Gütlich, P. *Struc. Bonding (Berlin)* **1981**, *44*, 83. (e) Goodwin, H. A. *Coord. Chem. Rev.* **1976**, *18*, 293. (f) Scheidt, W. R.; Reed, C. A. *Chem. Rev.* **1981**, *81*, 543. (g) König, E.; Ritter, G.; Kulshreshtha, S. K. *Chem. Rev.* **1985**, *85*, 219. (h) Bacci, M. *Coord. Chem. Rev.* **1988**, *86*, 245. (i) Gütlich, P. In *Chemical Mössbauer Spectroscopy*; Herber, R. H., Ed.; Plenum Press: New York, 1984. (j) Maeda, Y.; Takashima, Y. *Comments Inorg. Chem.* **1988**, *7*, 41.

(8) (a) Timken, M. D.; Strouse, C. E.; Soltis, S. M.; Daverio, S. A.; Hendrickson, D. N.; Abdel-Mawgoud, A. M.; Wilson, S. R. *J. Am. Chem. Soc.* **1986**, *108*, 395–402. (b) Federer, W. D.; Hendrickson, D. N. *Inorg. Chem.* **1984**, *23*, 3870–3877.

(9) (a) Finley, J. J.; Camley, R. E.; Vogel, E. E.; Zevin, V.; Gmelin, E. *Phys. Rev. B* **1981**, *24*, 1023. (b) Finley, J. J.; Nohl, H.; Vogel, E. E.; Imoto, H.; Camley, R. E.; Zevin, V.; Andersen, O. K.; Simon, A. *Phys. Rev. Lett.* **1981**, *46*, 1472. (c) Imoto, H.; Simon, A. *Inorg. Chem.* **1982**, *21*, 308.

(10) Bersuker, I. B.; Polinger, V. Z. Vibronic Interactions in Molecules and Crystals; Springer-Verlag: Berlin, 1989.

(11) (a) Webb, R. J.; Geib, S. J.; Staley, D. L.; Rheingold, A. L.; Hendrickson, D. N. *J. Am. Chem. Soc.* **1990**, *112*, 5031–5042, and references therein. (b) Jang, H. G.; Geib, S. J.; Kaneko, Y.; Nakano, M.; Sorai, M.; Rheingold, A. L.; Montez, B.; Hendrickson, D. N. *J. Am. Chem. Soc.* **1989**, *111*, 173–186, and references therein.

(12) (a) Christou, G. *Acc. Chem. Res.* **1989**, *22*, 328–335. (b) Vincent, J. B.; Christou, G. *Adv. Inorg. Chem.* **1989**, *33*, 197–257. (c) Brudvig, G. W.; Beck, W. F.; de Paula, J. C. *Annu. Rev. Biophys. Chem.* **1989**, *18*, 25. (d) Brudvig, G. W.; Crabtree, R. H. *Prog. Inorg. Chem.* **1989**, *37*, 99. (e) Wieghardt, K. *Angew. Chem., Int. Ed. Engl.* **1989**, *28*, 1153. (f) Pecoraro, V. L. *Photochem. Photobiol.* **1988**, *48*, 249. (f) Dismukes, G. C. In *Mixed Valency Systems: Applications in Chemistry, Physics and Biology*; Prassides, K., Ed.; Kluwer Academic Publishers: Dordrecht, 1991; pp 137–154. (g) Dismukes, G. C. *Chem. Scr.* **1988**, *28A*, 99–104. (h) Chan, M. K.; Armstrong, W. H. *J. Am. Chem. Soc.* **1991**, *113*, 5055.

(13) (a) Kok, B.; Forbush, B.; McGloin, M. *Photochem. Photobiol.* **1970**, *11*, 457. (b) Renger, G. *Angew. Chem., Int. Ed. Engl.* **1987**, *26*, 643.

(14) (a) Dismukes, G. C.; Siderer, Y. *Proc. Natl. Acad. Sci. U.S.A.* **1981**, *78*, 274–278. (b) Hansson, Ö.; Andréasson, L.-E. *Biochim. Biophys. Acta* **1982**, *679*, 261–268.

(15) (a) Casey, J. L.; Sauer, K. *Biochim. Biophys. Acta* **1984**, *767*, 21–28. (b) Zimmermann, J. L.; Rutherford, A. W. *Biochim. Biophys. Acta* **1984**, *767*, 160–167.

(16) (a) de Paula, J. C.; Brudvig, G. W. *J. Am. Chem. Soc.* **1985**, *107*, 2643–2648. (b) de Paula, J. C.; Beck, W. F.; Brudvig, G. W. *J. Am. Chem. Soc.* **1986**, *108*, 4002–4009. (c) de Paula, J. C.; Beck, W. F.; Miller, A.-F.; Wilson, R. B.; Brudvig, G. W. *J. Chem. Soc., Faraday Trans. 1* **1987**, *83*, 3635–3651.

(17) Hansson, Ö.; Aasa, R.; Vänngard, T. *Biophys. J.* **1987**, *51*, 825–832.

(18) Zimmermann, J. L.; Rutherford, A. W. *Biochemistry* **1986**, *25*, 4609–4615.

(19) Beck, W. F.; Brudvig, G. W. *Biochemistry* **1986**, *25*, 6479–6486.

(20) (a) de Paula, J. C.; Innes, J. B.; Brudvig, G. W. *Biochemistry* **1985**, *24*, 8114–8120. (b) Brudvig, G. W. In *Advanced EPR, Applications in Biology and Biochemistry*; Hoff, A. J., Ed.; Elsevier: Amsterdam, 1989; pp 839–865.

(21) Kim, D. H.; Britt, R. D.; Klein, M. P.; Sauer, K. *J. Am. Chem. Soc.* **1990**, *112*, 9389–9391.

(22) Diril, H.; Chang, H.-R.; Nilges, M. J.; Zhang, X.; Potenza, J. A.; Schugar, H. J.; Isied, S. S.; Hendrickson, D. N. *J. Am. Chem. Soc.* **1989**, *111*, 5102–5114, and references therein.

(23) Bashkin, J. S.; Chang, H.-R.; Streib, W. E.; Huffman, J. C.; Hendrickson, D. N.; Christou, G. *J. Am. Chem. Soc.* **1987**, *109*, 6502–6504.

(24) Li, Q.; Vincent, J. B.; Libby, E.; Chang, H.-R.; Huffman, J. C.; Boyd, P. D. W.; Christou, G.; Hendrickson, D. N. *Angew. Chem., Int. Ed. Engl.* **1988**, *27*, 1731–1733.

(25) Wang, S.; Folting, K.; Streib, W. E.; Schmitt, E. A.; McCusker, J. K.; Hendrickson, D. N.; Christou, G. *Angew. Chem., Int. Ed. Engl.* **1991**, *30*, 305–306.

S_1-state model complex, $[Mn_4O_2(O_2CCH_3)_6(py)_2(dbm)_2]$ (**4**), which has a Mn_4O_2 "butterfly" core[26] to the $Mn^{IV}Mn_3^{III}$ complex **3** has very recently been demonstrated.[25] Complexes **1**, **2**, and **3** have essentially superimposable distorted cubane Mn_4O_3Cl cores.

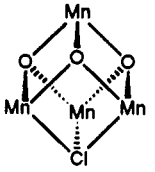

In a communication[24] we reported variable field magnetization data for complex **2**. From these data it was concluded that this $Mn^{IV}Mn_3^{III}O_3Cl$ complex has a relatively isolated $S = {}^9/_2$ ground state; the lowest energy excited state with $S = {}^7/_2$ was found at 226 cm^{-1} above the ground state. In this paper are reported the preparations, X-ray structures, ^1H NMR, magnetic susceptibility, and EPR results for complexes **1** and **2** and the new complexes $[Mn_4O_3Cl_4(O_2CCH_2CH_3)_3(py)_3]\cdot{}^5/_2(CH_3CN)$ (**4**) and $[Mn_4O_3Cl_4(O_2CCH_3)_3(HIm)_3]\cdot{}^5/_2(CH_3CN)$ (**5**).

Experimental Section

Syntheses. All manipulations were performed under aerobic conditions. All chemicals were used as received, except MeCN and Et_2O which were distilled prior to use for the preparation of **1**. $[Mn_3O(O_2CCH_3)_6(py)_3](ClO_4)$ and $[Mn_3O(O_2CH_2CH_3)_6(py)_3](ClO_4)$ were available from previous work.[27] Hydrated manganese(III) acetate, "$Mn(O_2CCH_3)_3\cdot 2H_2O$", was prepared by literature methods and slight modifications thereof.[28]

$(H_2Im)_2[Mn_4O_3Cl_6(O_2CCH_3)_3(HIm)]\cdot{}^3/_2CH_3CN$ (1). A stirred brown solution of $Mn(O_2CCH_3)_3\cdot 2H_2O$ (0.54 g, 2.0 mmol) in CH_3CN (20 mL) was treated dropwise with Me_3SiCl (0.66 mL, 5.2 mmol) to give a color change to purple-brown. A solution of imidazole (0.27 g, 4.0 mmol) in CH_3CN (15 mL) was added dropwise, and this resulted in a deep green solution and some brown precipitate. The latter was removed by filtration, a solution of $NaClO_4$ (0.29 g, 2.3 mmol) in CH_3CN (20 mL) was added to the filtrate, and the solution was refiltered to remove an off-white precipitate. The resulting red-brown filtrate was left undisturbed for several days at ambient temperature, and the resulting black crystals were collected by filtration, washed with CH_3CN and Et_2O, and dried in air. The yield is 20–30%, based on total available manganese. Anal. Calcd (Found) for $C_{18}H_{27.5}N_{7.5}O_9Cl_6Mn_4$: C, 23.36 (22.96); H, 3.00 (3.06); N, 11.35 (11.48); Cl, 22.98 (23.17); Mn, 23.75 (23.17).

$[Mn_4O_3Cl_4(O_2CCH_3)_3(py)_3]\cdot{}^3/_2CH_3CN$ (2). A stirred brown solution of $[Mn_3O(O_2CCH_3)_6(py)_3](ClO_4)$ (0.87 g, 1.00 mmol) in CH_3CN (50 mL) was treated with Me_3SiCl (0.70 mL, 5.5 mmol). The resulting red-brown solution was left undisturbed at ambient temperature for several days. The title compound formed as large red-brown crystals, together with a dirty yellow byproduct. The solids were collected by filtration, washed with EtOH (2 × 10 mL) to remove the yellow byproduct and then with CH_3CN (2 × 10 mL), and dried in air. The yield was 35–41% based on total available Mn. The scale of the reaction may be readily increased; one preparation was scaled up by a factor of 10^2 yielding approximately 30 g (~44%) of black crystals. Anal. Calcd (Found) for $C_{24}H_{28.5}N_{4.5}O_9Cl_4Mn_4$: C, 32.55 (32.4); H, 3.24 (3.2); N, 7.12 (7.15); Cl, 16.01 (16.1); Mn, 24.82 (24.7). Electronic spectrum in CH_2Cl_2: 254 (34 600), 340 (sh, 13 100), 570 (sh, 645). The $CD_3CO_2^-$ and C_5D_5N versions were prepared in an analogous manner from the appropriately deuterated Mn_3 starting material.

$[Mn_4O_3Cl_4(O_2CCH_2CH_3)_3(py)_3]\cdot{}^5/_2(CH_3CN)$ (4). A stirred brown solution of $[Mn_3O(O_2CCH_2CH_3)_6(py)_3](ClO_4)$ (0.95 g, 1.00 mmol) in CH_3CN (50 mL) was treated with Me_3SiCl (0.70 mL, 5.5 mmol). The resulting red-brown solution was filtered, and the filtrate was stored overnight at 5 °C. Dark red crystals formed, together with clear needles of a byproduct. The crystals were collected by filtration, washed with EtOH (to remove the byproduct) and MeCN, and dried in air. The yield was ~40% (based on total Mn). Anal. Calcd (Found) for $C_{29}H_{37.5}N_{5.5}O_9Cl_4Mn_4$: C, 35.96 (35.8); H, 3.90 (4.0); N, 7.95 (8.4); Cl, 14.64 (14.4).

$[Mn_4O_3Cl_4(O_2CCH_3)_3(HIm)_3]\cdot{}^5/_2(CH_3CN)$ (5). The previous procedure was followed until addition of Me_3SiCl. At this point, solid imidazole (0.20 g, 3.0 mmol) was added to give a green solution. The reaction mixture was filtered and left undisturbed for 2 days. The resulting dark red crystals were collected by filtration, washed with MeCN, and dried in air. The complex could not be obtained in analytical purity, but crystals were found that were suitable for structural characterization. The material is too insoluble for solution studies.

X-ray Crystallography. Data were collected on a Picker four-circle diffractometer at 115, 118, 130, and 128 K for complexes **1**, **2**, **4**, and **5**, respectively; details of diffractometry, low-temperature facilities, and computational procedures employed by the Molecular Structure Center are available elsewhere.[29] Data collection parameters are summarized in Table I for all four complexes.

Complex **1** crystallized as $(H_2Im)_2[Mn_4O_3Cl_6(O_2CCH_3)_3(HIm)]\cdot{}^3/_2CH_3CN$. An approximately equidimensional crystal was mounted using silicone grease. Systematic absences uniquely determined the space group as *Pbca*. Four standards measured every 300 reflections appeared to have a systematic drift. The residual for the averaging of 832 intensities observed more than once was 0.045 after correction for the drift. The structure was solved by a combination of direct methods (MULTAN78), Fourier techniques, and chemical information. The non-hydrogen atoms of the anion, assumed to be $[Mn_4Cl_6O_3(O_2CCH_3)_3(C_3N_2H_4)]^{2-}$, were located and these refined well. In addition, two five-membered rings were located and were assumed to be $C_3N_2H_5^+$ cations. These cations were found to be disordered about pseudo-5-fold axes and were refined as C_5 rings. The CH_3CN solvate molecule was also found to be disordered and was refined as one carbon atom of full occupancy and four carbon atoms of half occupancy. Hydrogen atoms were placed in fixed calculated positions for the anion to improve its refinement. The final difference map had numerous small peaks, the largest of which was 0.78 e/Å^3.

Complex **2** crystallizes as $[Mn_4O_3Cl_4(O_2CCH_3)_3(py)_3]\cdot 4CH_3CN$. A crystal was transferred to the goniostat using standard inert atmosphere handling techniques and cooled to 118 K. A systematic search of the limited hemisphere of reciprocal space located a set of diffraction maxima with symmetry and systematic absences corresponding to a rhombohedral-centered hexagonal cell. The cell was indexed as rhombohedral and subsequent solution and refinement confirmed the space group to be $R\bar{3}$. The structure was solved by a combination of direct methods (MULTAN78) and Fourier techniques. The positions of all nonsolvent hydrogen atoms were clearly visible in a different Fourier phased on the non-hydrogen atoms, and the coordinates and isotropic thermal parameters for hydrogen atoms were varied in the final cycles of refinement. Two independent CH_3CN solvent molecules were located in the asymmetric cell. One lies in a general position, while the other with approximately 50% occupancy lies on the 3-fold axis. It was not possible to locate the hydrogen atoms associated with the solvate molecules. A final difference Fourier was essentially featureless, with the largest peaks being 0.63 e/Å^3, all associated with the solvate molecules on the 3-fold axis.

Complex **4** crystallizes as $[Mn_4O_3Cl_4(O_2CCH_2CH_3)_3(py)_3]\cdot{}^5/_2CH_3CN$. A small, almost equidimensional crystal was selected from the bulk sample and transferred to the goniostat where it was cooled to 130 K. A systematic search of a limited hemisphere of reciprocal space yielded a set of reflections which exhibited $R\bar{3}$ diffraction symmetry. The reflections were indexed using an R-centered hexagonal unit cell of $a = b = 15.921$ Å, $c = 28.229$ Å, and $\cos\gamma = 0.500$. No correction for absorption was performed. The structure was solved by using the usual combination of direct methods and Fourier techniques. The structure was solved using the hexagonal setting. However, since complex **4** was found to be isostructural to complex **2**, the unit cell was switched to the rhombohedral primitive space group $R\bar{3}$; the unit cell parameters are given in Table I. The non-hydrogen atoms were readily located in a difference Fourier phased with the Mn and Cl atoms. All hydrogen atoms on the Mn complex were located. As with complex **2**, complex **4** crystallizes with CH_3CN, one molecule in a general position and one of the 3-fold axis. The full matrix least-squares refinement was completed using anisotropic thermal parameters on the 16 unique atoms in the Mn complex and on the CH_3CN in the general position. The hydrogen atoms were varied using isotropic thermal parameters. No hydrogen atoms were introduced on the solvate molecules. The final difference Fourier was essentially featureless with the largest peak being 0.89 e/Å^3 in close proximity to N(20) of the CH_3CN solvate molecule on the 3-fold axis.

Complex **5** crystallizes as $[Mn_4O_3Cl_4(O_2CCH_3)_3(HIm)_3]\cdot x CH_3CN$. An approximately equidimensional crystal was mounted using silicone grease and was transferred to a goniostat where it was cooled to 128 K for characterization and data collection. Laue symmetry and systematic absences in the intensity data determined the space group to be $R3$ or $R\bar{3}$. The space group $R\bar{3}$ was chosen and was confirmed by the successful

(26) Vincent, J. B.; Christmas, C.; Chang, H.-R.; Li, Q.; Boyd, P. D. W.; Huffman, J. C.; Hendrickson, D. N.; Christou, G. *J. Am. Chem. Soc.* **1989**, *111*, 2086–2097.

(27) Vincent, J. B.; Chang, H.-R.; Folting, K.; Huffman, J. C.; Christou, G.; Hendrickson, D. N. *J. Am. Chem. Soc.* **1987**, *109*, 5703–5711.

(28) Bush, J. B., Jr.; Finkbeiner, H. *J. Am. Chem. Soc.* **1968**, *90*, 5903.

(29) Chisholm, M. H.; Folting, K.; Huffman, J. C.; Kirkpatrick, C. C. *Inorg. Chem.* **1984**, *23*, 1021.

structure determination. Four standards measured every 300 reflections showed no significant trends. The residual for the averaging of redundant data was 0.048 for 1677 unique data, all of which were measured more than once. The structure was solved by a combination of direct methods (MULTAN78) and Fourier techniques. The atoms in the molecule of interest were easily located; however, the difference maps had molecules of CH_3CN solvent. Two of these molecules have close contacts of 1.9 Å and this, together with the low peak height clearly indicated partial occupancy at more than one location as well as the probable solvent loss observed in other crystals. To improve the refinement of the molecule of interest, two solvent molecules at $^1/_3$ weight and one additional carbon atom at a third location at $^1/_3$ weight were included in the least-squares calculations. A difference map then revealed most of the hydrogen atoms, most importantly the relative position of the hydrogen atoms on the $CH_3CO_2^-$ ligands. Calculated fixed hydrogen atom positions were used in the final least squares refinement which had a residual of 0.0575. The final difference map had no significant additional peaks, the largest being 0.86 e/Å^3.

Physical Measurements. The temperature dependent magnetic susceptibilities of complexes **1**, **2**, and **4** were measured using a series 800 VTS-50 SQUID susceptometer (S.H.E. Corporation). Data were collected from 5–300 K at 10 kG for each compound. Data were also collected from 2–40 K at magnetic fields of 24.8, 34.5, and 44.0 kG for complex **2** and at magnetic fields of 10.0, 30.0, and 48.0 kG for complex **4**. Pascal's constants[30] were used to estimate the diamagnetic correction for each complex, which were subtracted from the experimental susceptibilities to give the molar paramagnetic susceptibilities.

X-band EPR spectra were recorded with a Bruker ER200D spectrometer. Q-band EPR spectra were recorded with a Varian E15 Q-band spectrometer. Both spectrometers were equipped with a EIP 548A frequency meter and a Varian E-500 NMR gauss meter. Frozen glass samples were prepared by dissolving the compounds in the appropriate spectroscopic grade solvents and then freezing the samples at liquid-nitrogen temperature. Infrared (Nujol mull) and electronic absorption solution spectra were recorded on a Nicolet Model 510P and Hewlett-Packard Model 8452A spectrophotometers, respectively. ^{1}H NMR spectra were recorded on a Varian XL-300 spectrometer. Chemical shifts are quoted on the δ scale (downfield shifts are positive).

Results and Discussion

Syntheses. Previous work has established that $[Mn_3O(O_2CR)_6(py)_3](ClO_4)$ (R = various substituents) and related species represent an excellent entry point into higher nuclearity $Mn/O/RCO_2^-$ aggregates.[24,26,31] Of particular relevance is the observation that bpy causes a nuclearity change from three to four.[26] The present work is an extension along similar lines. In the same way that bidentate bpy with its restricted bite angle cannot bind to Mn_3O species without a resulting serious structural perturbation, it was reasoned that carboxylate abstraction from a trinuclear complex would also necessitate a drastic structural/nuclearity change. As in the bpy reactions, it could not be anticipated what the products might be. The carboxylate-abstraction reagent Me_3SiCl[32] was chosen, and initial experiments employed polymeric manganese(III) acetate "$Mn(O_2CCH_3)_2 \cdot 2H_2O$".

Treatment of Mn^{III} acetate in CH_3CN with, sequentially, Me_3SiCl (2.6 equiv), imidazole, and $NaClO_4$ yielded a variety of color changes and, finally, a red-brown solution that slowly deposited black crystals of $(H_2Im)_2[Mn_4O_3Cl_6(O_2CCH_3)_3(HIm)]\cdot{}^3/_2MeCN$ (**1**) in analytical purity. The latter was important, for the material is only sparingly soluble and thus not amenable to recrystallization. With the identity of complex **1** established, attempts to optimize yield and simplify the procedure by omission of $NaClO_4$ led only to a failure to obtain **1**. Successful preparation of **1** is, however, fully reproducible with the procedure described.

Charge considerations indicate a mixed-valence $Mn_3^{III}Mn^{IV}$ description for complex **1**, assuming that nonbound imidazoles are protonated and bridging oxygen atoms are not. In confirmation of this, iodometric redox titrations gave an average metal oxidation state in the range 3.2–3.3 from multiple determinations.[33] The origin of the Mn^{IV} is most likely disproportionation of Mn^{III}. The logical disproportionation equation (eq 1) would predict a

$$5Mn_3^{III} \rightarrow 3Mn_3^{III}Mn^{IV} + 3Mn^{II} \quad (1)$$

maximum yield of **1** of 80%, but we believe that the amount of manganese is not the yield-determining factor and that eq 1 is not an accurate representation of the reaction (vide infra).

The formation of **1** from Mn_3O species obviously involves a complex reaction sequence, leading as it does to changes in nuclearity, oxidation level and oxide/Mn ratio. To probe various aspects of this reaction further a more convenient reaction system was deemed necessary and subsequently developed. Treatment of $[Mn_3O(O_2CCH_3)_6(py)_3](ClO_4)$ with Me_3SiCl was found to lead to a similar transformation and the isolation of neutral $[Mn_4O_3Cl_4(O_2CCH_3)_3(py)_3]\cdot{}^3/_2MeCN$ (**2**), which is also sparingly soluble. This two-reagent system was more amenable to detailed study. The Me_3SiCl/Mn_3O ratio was varied in increments from 2:1 to 12:1 with other factors (reaction time, concentration, reaction under N_2) kept constant, and an optimum yield was obtained at a 5:1 ratio. The other ratios gave decreased yields of **2** but *no* other precipitated product except for a Mn^{II} byproduct. The latter was observed co-precipitating with **2** at all reaction ratios (but is easily removed by washing) and provided direct evidence for a disproportionation.[34] The reaction (5:1 ratio) was nevertheless carried out under N_2 using rigorously distilled and degassed CH_3CN; the reaction again gave **2** in comparable yield. We feel confident that Mn^{IV} is not arising through aerial oxidation of Mn^{III}. At the other extreme, the reaction was performed in air using CH_3CN as received and a slightly increased reaction ratio (5.5:1) to compensate for the presence of water; again, comparable yields of **1** were obtained, and the latter, more convenient procedure is now the one employed on a routine basis.

Addition of imidazole to the solution after addition of Me_3SiCl (but before **2** begins to crystallize) instead gives $[Mn_4O_3Cl_4(O_2CCH_3)_3(HIm)_3)]$ (**5**). This complex was obtained in less-than-acceptable purity[35] and is even less soluble than **1** or **2**; its study was, therefore, limited to crystallographic characterization. The preparative procedure to **2** may be extended even further; use of $[Mn_3O(O_2CCH_2CH_3)_6(py)_3](ClO_4)$ was found to give pure $[Mn_4O_3Cl_4(O_2CCH_2CH_3)_3(py)_3]$ (**4**) in ~40% yield. Complex **4** is only slightly more soluble than **2**. Attempts to prepare complexes with larger R groups (e.g., $PhCO_2^-$) have failed to produce characterizable products.

It is important to propose at least a partial rationalization for the 5:1 optimum reaction ratio and concomitant yields consistently in the ~40% range. On the basis of the 5:1 ratio, balanced eq 2 can be formulated.

$$3[Mn_3O(O_2CCH_3)_6(py)_3]^+ + 15Me_3SiCl \rightarrow 15Me_3SiO_2CMe + [Mn_4O_3Cl_4(O_2CCH_3)_3(py)_3] + 6py + 4Mn^{3+} + Mn^{2+} + 11Cl^- \quad (2)$$

A simplified form of eq 2 is eq 3. We believe that eq 3 rather than eq 1 better summarizes the overall reaction; if so, this suggests

$$3Mn_3O^{7+} \rightarrow Mn_4O_3^{7+} + 4Mn^{3+} + Mn^{2+} \quad (3)$$

that the maximum possible yield of **2** is 44.4%, which is satisfyingly close to experimental values. Further, no additional oxides are required, consistent with no change in yield when anhydrous conditions are imposed, and the remaining Mn^{3+} in solution would rationalize the colored nature of the mother liquor after collection of sparingly soluble product crystals by filtration.[36] The yield

(30) *Theory and Applications of Molecular Paramagnetism*; Boudreaux, E. A., Mulay, L. N., Eds.; Wiley and Sons, Inc.: New York, 1976.

(31) Libby, E.; McCusker, J. K.; Schmitt, E. A.; Folting, K.; Huffman, J. C.; Hendrickson, D. N.; Christou, G. *Inorg. Chem.* **1991**, *30*, 3486–3495.

(32) (a) McCarley, R. E.; Ryan, T. R.; Torardi, C. C. *ACS Symp. Ser.* **1981**, *155*, 41. (b) Green, M. L. H.; Parkin, G.; Bashkin, J.; Fail, J.; Prout, K. *J. Chem. Soc., Dalton Trans.* **1982**, 2519.

(33) Samples of **1** (15–20 mg) were decomposed in acidic KI solution, and the resulting I_3^- was titrated against satandardized thiosulfate.

(34) Solid obtained from the EtOH wash solution analyzed with a Mn/Cl ratio of 1:2 and small amounts of N, suggesting a solvated $MnCl_2$ derivative with traces of pyridine.

(35) We believe **5** is contaminated with **2** or mixed HIm/py versions. Pure **5** might be attainable by increasing the amount of added HIm, but, given the low solubility of **5**, this has not been pursued.

Table I. Crystallographic Data for Complexes **1**, **2**, **4**, and **5**

	1	2	4	5
formula	$C_{18}H_{27.5}N_{7.5}O_9Cl_6Mn_4$	$C_{29}H_{36}N_7O_9Cl_4Mn_4$	$C_{32}H_{42}NO_9Cl_4Mn_4$	$C_{15}H_{21}N_6O_9Cl_4Mn_4$[a]
Mr	925.43	988.22	1030.30	790.94
cryst system	orthorhombic	hexagonal	hexagonal	hexagonal
space group	*Pbca*	$R\bar{3}$	$R\bar{3}$	$R\bar{3}$
temp, °C	−158	−155	−143	−145
a, Å	14.307 (14)	13.031 (4)	13.156 (6)	15.656 (6)
b, Å	14.668 (14)	13.031 (4)	13.156 (6)	15.656 (5)
c, Å	31.319 (36)	13.031 (4)	13.156 (6)	26.947 (9)
α, deg	90.0	74.81 (2)	74.56 (3)	90.0
β, deg	90.0	74.81 (2)	74.56 (3)	90.0
γ, deg	90.0	74.81	74.56 (3)	120.0
Z	8	2	2	6
V, Å^3	6572.75	2015.93	2068.53	5722.68
cryst dimens, mm	0.5 × 0.50 × 0.50	0.3 × 0.30 × 0.30	0.20 × 0.25 × 0.25	0.20 × 0.25 × 0.25
radiation, Å	0.71069[b]	0.7106[b]	0.7106[b]	0.71069[b]
abs coeff, cm^{-1}	9.304	14.982	14.636	15.739
scan speed, deg/min	6.0	4.0	4.0	4.0
scan width, deg	1.3 + dispersion	2.0 + dispersion	1.8 + dispersion	1.8 + dispersion
data collcd	6° ≤ 2θ ≤ 45°	6° ≤ 2θ ≤ 45°	6° ≤ 2θ ≤ 45°	5° ≤ 2θ ≤ 45°
total data	5807	5577	4409	7123
unique data	4312	1759	1813	1677
averaging *R*[c]	0.045	0.045	0.052	0.048
obsd data	2513[d]	1458[e]	1425[e]	1156[e]
$100R(R_w)$[b]	8.10 (8.70)	3.71 (4.17)	5.25 (5.44)	5.75 (5.90)
goodness of fit[g]	1.821	1.062	1.282	1.193

[a] Excluding solvent molecules. [b] Mo Kα, graphite monochromator. [c] For reflections measured more than once. [d] $F > 2.336(F)$. [e] $F > 3.06(F)$. [f] $R = \sum||F_o| - |F_c||/\sum|F_o|$. $R_w = [\sum w(|F_o| - |F_c|)^2/\sum w|F_o|^2]^{1/2}$ where $w = 1/\sigma^2(|F_o|)$. [g] Goodness of fit = $[\sum w(|F_o| - |F_c|)^2/(N_{obsns} - N_{paras})]^{1/2}$.

may, thus, be acetate/oxide-limited,[37] and experimental yields of **2** (and **4**) may, in fact, be essentially quantitative. Additional support for this proposal is provided by recent work that has shown that addition of acetic acid and water to the reaction solution *after* addition of Me_3SiCl leads to a new $[Mn_4O_3Cl]^{6+}$-containing complex *in 75% yield based on eq 1* (maximum possible yield 80% based on Mn).

Overall, it is reasonable to propose that the Me_3SiCl removes five of the six $MeCO_2^-$ groups; this highly destabilizes the Mn_3O unit, presumably causing fragmentation, followed by an undoubtedly complex series of steps including disproportionation and rearrangement, finally to assemble an $[Mn_4O_3Cl]^{6+}$ product. It is paradoxical that the reaction is triggered by carboxylate-abstraction, and yet the yield of product is carboxylate-dependent.[37] Higher ratios of Me_3SiCl decrease the yield, as would be expected from eqs 2 and 3; lower ratios of Me_3SiCl also decrease the yield, presumably because sufficient carboxylate is available to stabilize Mn^{III} species (including starting material) and thus decrease the extent of disproportionation/rearrangement that leads to **2**.

Description of Structures. An ORTEP projection of the $Mn^{IV}Mn_3^{III}$ anion in complex **1** is shown in Figure 1, while Figure 2 shows ORTEP projections for complexes **2**, **4**, and **5**. Complex **1**, $(H_2Im)_2[Mn_4O_3Cl_6(O_2CCH_3)_3(HIm)]\cdot{}^3/_2CH_3CN$, crystallizes in the orthorhombic space group *Pbca*. The asymmetric unit contains a complete anion along with two $C_3N_2H_5^+$ cations and one CH_3CN solvent molecule. The solvent molecule will not be further discussed. The $C_3N_2H_5^+$ imidazolium cations are disordered. In the refinement the N atoms could not be distinguished from the C atoms, necessitating refinement of the cations as C_5 rings. The central $[Mn_4(\mu_3\text{-}O)_3(\mu_3\text{-}Cl)]^{6+}$ core of the anion in complex **1** is best considered as a Mn_4 pyramid with the Mn^{IV} ion Mn(1) at the apex, a μ_3-Cl atom Cl(5) bridging the basal plane, and a μ_3-O bridging each of the remaining three faces (Figure 1). Alternatively, the core of complex **1** can be described as a severely distorted Mn_4O_3Cl cubane. The unique HIm ligand destroys the idealized C_{3v} symmetry. The Mn···Mn separations fall into two types. The average Mn(1)···Mn(2,3,4) distance of 2.814 Å is distinctly shorter than those between the Mn^{III} ions (av = 3.285 Å). In Table II are summarized selected bond distances and angles for the anion in complex **1**.

The three Mn^{III} ions and the one Mn^{IV} ion in the anion of complex **1** have distorted octahedral coordination geometries.

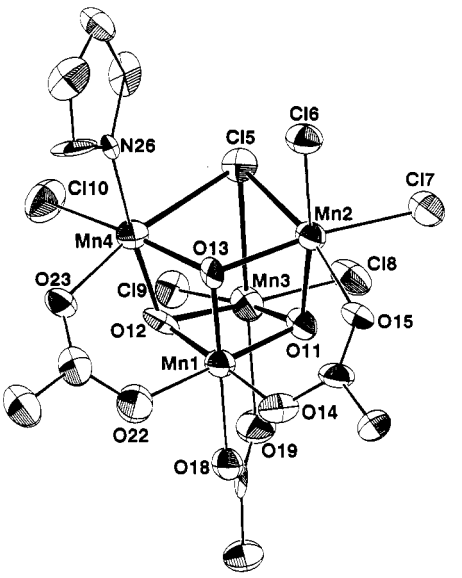

Figure 1. ORTEP plot for the anion of $(H_2Im)_2[Mn_4O_3Cl_6(O_2CCH_3)_3(HIm)]\cdot{}^3/_2CH_3CN$ (**1**).

Table II. Comparative Structural Parameters (Å or deg) for $[Mn_4O_3Cl]^{6+}$ Complexes **1**, **2**, **4**, and **5**[a]

parameter[b]	1[c]	2	4	5
$Mn^{III}\cdots Mn^{IV}$	2.814 (8)	2.815 (2)	2.814 (2)	2.803 (2)
$Mn^{III}\cdots Mn^{III}$	3.285 (39)	3.269 (2)	3.271 (2)	3.265 (2)
Mn^{IV}–O_b	1.833 (36)	1.865 (3)	1.870 (4)	1.856 (6)
Mn^{III}–O_b[d]	1.979 (24)	1.966 (3)	1.962 (5)	1.965 (6)
Mn^{III}–O_b[e]	1.885 (13)[f]	1.922 (3)	1.924 (5)	1.920 (6)
Mn^{III}–Cl_b	2.624 (16)	2.627 (2)	2.630 (2)	2.614 (3)
Mn^{IV}–O_A	1.955 (5)	1.950 (3)	1.945 (5)	1.951 (6)
Mn_{III}–O_A	2.185 (4)	2.146 (3)	2.158 (5)	2.140 (6)
Mn^{III}–Cl_t	2.266 (15)	2.237 (2)	2.236 (3)	2.242 (3)
Mn^{III}–N	1.978 (16)[f]	2.045 (4)	2.049 (6)	2.019 (7)
O_b–Mn^{IV}–O_b	86.2 (1.8)	84.94 (15)	84.90 (20)	85.41 (26)
O_b–Mn^{III}–O_b	79.3 (10)	80.77 (19)	81.03 (26)	80.80 (30)
Cl_b–Mn^{III}–O_b[b]	84.0 (6)	83.85 (11)	83.84 (14)	83.75 (18)
Cl_b–Mn^{III}–O_b[e]	86.6 (4)[f]	84.70 (11)	84.55 (14)	84.61 (18)
Cl_b–Mn^{III}–Cl_t	95.0 (37)	96.34 (5)	95.68 (7)	94.67 (9)
Cl_b–Mn^{III}–N	93.5 (5)[f]	89.87 (12)	90.15 (17)	90.73 (21)
Cl_b–Mn^{III}–O_A	168.8 (8)	168.69 (10)	169.02 (14)	169.14 (19)
Cl_b–Mn^{III}–O_b	172.1 (13)	173.73 (11)	174.21 (15)	173.96 (20)
Cl_t–Mn^{III}–O_b	93.3 (14)	93.00 (11)	93.18 (15)	93.27 (19)
Cl_t–Mn^{III}N	93.5 (5)[f]	95.02 (3)	94.81 (18)	94.74 (22)
Cl_t–$Mn^{III}O_A$	92.9 (40)	94.68 (11)	95.02 (15)	95.75 (19)
N–Mn^{III}–O_b	94.0 (6)[f]	91.25 (16)	90.96 (22)	91.11 (26)
N–Mn^{III}–O_b[e]	173.4 (6)[f]	170.77 (16)	170.81 (23)	171.04 (27)
N–Mn^{III}–O_A	89.5 (6)[f]	91.69 (15)	91.41 (22)	91.45 (27)
O_A–Mn^{III}–O_b[d]	87.1 (36)	84.92 (13)	85.26 (19)	85.57 (24)
O_A–Mn^{III}–O_b[e]	89.1 (6)[f]	92.21 (13)	92.40 (29)	91.74 (24)
O_a–Mn^{IV}–O_A	86.2 (16)	87.01 (15)	87.35 (20)	86.40 (50)
O_A–Mn^{IV}–O_b	178.0 (10)	176.78 (15)	176.91 (20)	177.56 (26)
O_A–Mn^{IV}–O_b	93.5 (11)	92.08 (14)	92.12 (20)	92.52 (26)
O_A–Mn^{IV}–O_b	94.1 (8)	96.03 (14)	95.67 (20)	95.72 (25)
Mn^{IV}–O_b–Mn^{III}[d]	95.3 (20)	94.51 (15)	94.49 (21)	94.32 (15)
Mn^{IV}–O_b–Mn^{III}[e]	97.1 (6)[f]	96.00 (15)	95.74 (21)	95.84 (26)
Mn^{III}–O_b–Mn^{III}	113.5 (6)	114.48 (17)	114.66 (22)	114.36 (28)
Mn^{III}–Cl_b–Mn^{III}	77.5 (1.0)	76.97 (6)	76.91 (5)	77.27 (10)

[a] See supplementary material for full listings. [b] b = bridging, t = terminal, A = carboxylate. [c] Average values quoted; number in parentheses is the maximum deviation from the average. [d] Atom trans to Cl. [e] Atom trans to N. [f] Single value; number in parentheses is the esd.

(36) The nature of the colored species left in solution is unclear, but it is reasonable to assume these are Mn^{III}/Cl/py species, mononuclear or otherwise.

(37) Since it is possible to remove all sources of oxide (water, glass surfaces, etc.), the carboxylate is likely the most important yield-limiting factor.

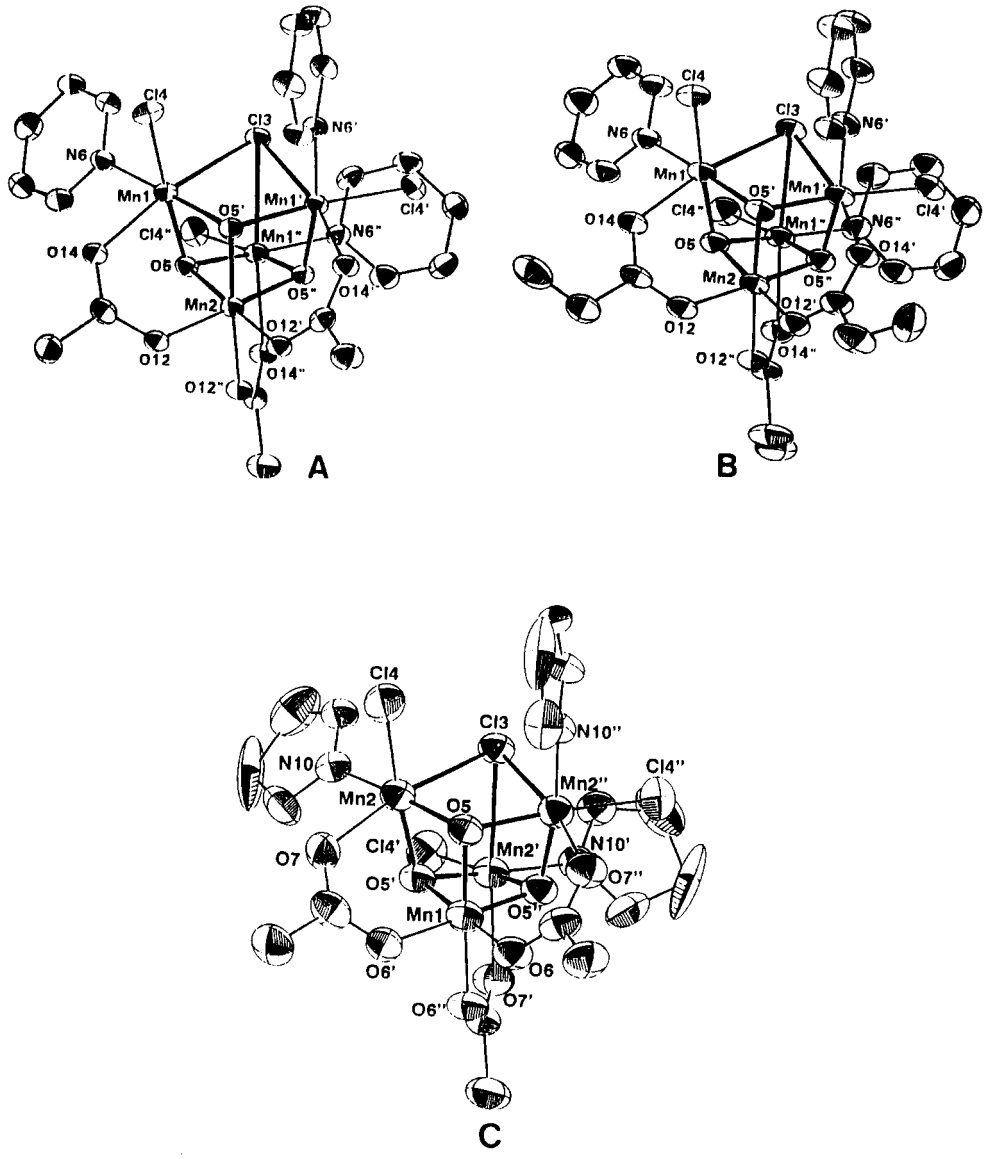

Figure 2. ORTEP plots of the $Mn^{IV}Mn_3^{III}$ complexes in isostructural (A) $[Mn_4O_3Cl_4(O_2CCH_3)_3(py)_3]\cdot{}^3/_2CH_3CN$ (**2**), (B) $[Mn_4O_3Cl_4(O_2CCH_2CH_3)_3(py)_3]\cdot{}^5/_2CH_3CN$ (**4**), and (C) $[Mn_4O_3Cl_4(O_2CCH_3)_3(HIm)_3]\cdot{}^5/_2CH_3CN$ (**5**).

Ligation about the Mn^{IV} ion, Mn(1), is comprised of six O atoms, three of which are from the three μ_3-O^{2-} ions and the other three from the three bridging acetate ions. Two of the Mn^{III} ions [Mn(2) and Mn(3)] have $Mn(Cl)_2(\mu_3\text{-}Cl)(\mu_3\text{-}O)_2(\mu\text{-}O_2CCH_3)$ coordination spheres, whereas for the third Mn^{III} ion, Mn(4), one of the terminal Cl^- ligands is replaced by an imidazole ligand. Each of the three Mn^{III} ions exhibits a Jahn–Teller distortion (elongation) along the (μ_3-Cl)–Mn^{III}–O(acetate) axis. In the case of Mn(3), for example, the Mn(3)–O(19)acetate bond distance is 2.198 (15) Å, which is long for a Mn^{III}–O(acetate) bond and is characteristic of a Jahn–Teller distortion axis. For the butterfly complex $[Mn_4^{III}O_2(O_2CCH_3)_7(bpy)_2](ClO_4)$, the Mn^{III}–O(acetate) distances which define the Jahn–Teller distortion axes are in the range of 2.184 (20) to 2.259 (19) Å, whereas the other Mn^{III}–O(acetate) distances fall in the range of 1.937 (13) to 1.970 (16) Å.[26] Thus, all three Mn^{III} ions in complex **1** have their Jahn–Teller z-axes directed at the same μ_3-Cl ion, Cl(5).

Complexes **2**, **4**, and **5** crystallize in the rhombohedral space group $R\bar{3}$. There are CH_3CN solvate molecules present in each of these complexes, and these will not be further discussed. Each of these $Mn^{IV}Mn_3^{III}$ complexes has crystallographically imposed C_3 symmetry (Figure 2). The Mn_4O_3Cl cores of these three complexes are nearly identical and are also essentially superimposable with that of complex **1**. For comparison with complex **1** it can be noted that the Mn···Mn separations for complex **2** are Mn^{IV}···Mn^{III} = 2.815 (2) Å and Mn^{III}···Mn^{III} = 3.269 (2) Å. In all four complexes the bridging Mn–Cl distances are appreciably longer than Mn–Cl terminal distances, a point of relevance to the question of the possible presence of Cl^- ligands in any of the S_n states of PSII as examined in EXAFS studies.[38] As with complex **1**, it is clear from the metric details given in Table II that the Jahn–Teller distortion axis for each Mn^{III} ion in complex **2** lies along the (μ_3-Cl)–Mn^{III}–O(acetate) axis. Obviously complexes **2** and **4** only differ in the identity of the carboxylate bridging group. Since imidazole is a more biologically relevant ligand than pyridine, the complex $[Mn_4O_3Cl_4(O_2CCH_3)_3(HIm)_3]$ (**5**) was prepared and also found to crystallize in the $R\bar{3}$ space group. Examination of the metric details in Table II shows that this complex is quite similar to the pyridine analogue complex **2**.

In the absence of a single crystal X-ray structure characterizing the Mn_4 active site in PSII, the best structural data for the Mn_4 complex has come from EXAFS studies.[38] These studies give

(38) (a) Penner-Hahn, J. E.; Fronko, R. M.; Pecoraro, V. L.; Yocum, C. F.; Betts, S. D.; Bowlby, N. R. *J. Am. Chem. Soc.* **1990**, *112*, 2549. (b) George, G. N.; Prince, R. C.; Cramer, S. P. *Science* **1989**, *243*, 789. (c) Guiles, R. D.; Zimmermann, J.-L.; McDermott, A. E.; Yachandra, V. K.; Cole, J. L.; Dexheimer, S. L.; Britt, R. D.; Wieghardt, K.; Bossek, U.; Sauer, K.; Klein, M. P. *Biochemistry* **1990**, *29*, 471. (d) Guiles, R. D.; Yachandra, V. K.; McDermott, A. E.; Cole, J. L.; Dexheimer, S. L.; Britt, R. D.; Sauer, K.; Klein, M. P. *Biochemistry* **1990**, *29*, 486. (e) Yachandra, V. K.; Guiles, R. D.; McDermott, A. E.; Cole, J. L.; Britt, R. D.; Dexheimer, S. L.; Sauer, K.; Klein, M. P. *Biochemistry* **1987**, *26*, 5974.

Table III. Selected IR Spectral Data[a] for Complexes **1**, **2**, **4**, and **5**

stretch	**1**	**2**	**4**	**5**
ν_{as}(COO)	1555[b]	1564	1555	1564
	~1540 (sh)[b]	1549	~1545 (sh)	1550
ν_{M-O}	608[c]	615	610	613
	580[b]	586	585	588
	510[c]	519	515	513
	425 (br)[d]	438	445	438

[a] ±4 cm^{-1}. [b] Strong. [c] Medium. [d] Weak.

information about the Mn coordination spheres in terms of types of atoms, number of atoms, and interatomic distances. Recent EXAFS data for the S_1 and S_2 states indicate that there are 2–3 Mn···Mn interactions at 2.7 Å and 1–2 Mn···Mn interactions at 3.3 Å. Penner-Hahn and co-workers[38a] note, however, that a larger number of 3.3 Å interactions cannot be excluded based upon their data.[38a] For complexes **1**, **2**, **4**, and **5** there are three Mn^{III}·Mn^{IV} interactions at ~2.8 Å and three Mn^{III}···Mn^{III} interactions at ~3.3 Å. The EXAFS data for WOC Mn_4 site also suggests that there are two types of O (or N) ligands at distances of 1.9 and 2.1 Å.[38a] From Table II it is apparent that for complexes **1**, **2**, **4**, and **5** there are several Mn–O (and/or N) bond distances within the range 1.8–2.2 Å. Although the precise role of chloride in the Mn_4 active site PSII is not understood, its presence is well documented. There is no direct experimental evidence for chloride coordination to Mn. EXAFS data rule out Mn···Cl chloride interactions at <2.3 Å, but EXAFS signal-to-noise ratios prevent the detection of Mn···Cl interactions at distances >2.3 Å. The terminal Cl atoms coordinated to the Mn^{III} ions in complexes **1**, **2**, **4**, and **5** have Mn–Cl bond distances at ~2.25 Å and are most likely not present in the WOC. The three Mn^{III}–μ_3-Cl distances which are a part of the cubane core are ~2.62 Å. If this Mn^{III}–μ_3-Cl substructure were a part of the S_2 state, it is unlikely that it could be readily detected by EXAFS studies. Finally, it is important to note that the μ_3-Cl in complexes **1**, **2**, **4**, and **5** causes a distortion of the cubane structure which is important since, as Penner-Hahn et al.[38a] have pointed out, a regular cubane would be inconsistent with current EXAFS and XANES data.

Structural Comparisons with $[Mn_4O_2]^{8+}$ Complexes and Biological Implications. In previous reports,[26,31] we have described the structures of the Mn_4^{III} "butterfly" complexes $[Mn_4O_2(OAc)_7(bpy)_2]^+$ (**6**, bpy = 2,2′-bipyridine) and $[Mn_4O_2(OAc)_7(pic)_2]^-$ (**7**, pic = picolinate) and shown that they are essentially superimposable. These complexes were proposed as potential models for the S_1 state of the native water oxidation center (WOC).[26,31,39] Further, the lower oxidation state complexes $[Mn_4O_2(O_2CPh)_7(bpy)_2]$ (**8** = Mn^{II}, 3 Mn^{III}) and $[Mn_4O_2(OAc)_6(bpy)_2]$ (**9**, 2 Mn^{II}, 2 Mn^{III}) were proposed[26] as models for the S_0 and S_{-1} states, respectively (eq 4). The preparation

$$\underset{\substack{2Mn^{II},2Mn^{III}\\ \mathbf{9}}}{[Mn_4O_2]^{6+}} \xrightarrow{-e^-} \underset{\substack{Mn^{II},3Mn^{III}\\ \mathbf{8}}}{[Mn_4O_2]^{7+}} \xrightarrow{-e^-} \underset{\substack{4Mn^{III}\\ \mathbf{7,6}}}{[Mn_4O_2]^{8+}} \quad (4)$$

of the $[Mn_4O_3Cl]^{6+}$ cubane complexes with oxidation level $3Mn^{III},Mn^{IV}$ provides the initial examples of Mn_4 species at this level and invites their proposal as models for the S_2 state; these ideas were incorporated into one of the mechanistic schemes that we have put forward for the catalytic cycle of the WOC.[39]

Although the cubane complexes differ from **6** and **7** by the necessary single oxidation state unit, the apparently large difference in structure between the butterfly $[Mn_4O_2]^{8+}$ and cubane $[Mn_4O_3Cl]^{6+}$ cores might seem to rule out their occupation of adjacent S_n states of the WOC cycle. However, these two structural motifs are not as different as first impressions might suggest; the $[Mn_4O_3Cl]^{6+}$ core contains as a substructure the "Mn_4O_2" butterfly unit. If we use complex **2** for further discussion, the view of the latter complex in Figure 2 was deliberately chosen to emphasize this similarity. The substructure defined by Mn(1), Mn(1′), Mn(1″), Mn(2), O(5), and O(5″) represents an Mn_4O_2 butterfly unit. The Mn_4O_2 core of **6** and **7** can thus be related to the Mn_4O_3 unit in **2** by addition of the third oxide O(5′) to bridge Mn(1), Mn(1′), and Mn(2). Since the substrate of the WOC is H_2O and the latter is merely protonated oxide, it is attractive to propose that conversion of a putative Mn_4O_2 unit at S_1 to an Mn_4O_3Cl unit at S_2 would involve incorporation of deprotonated H_2O at position O(5′) (eq 5) (together with addition

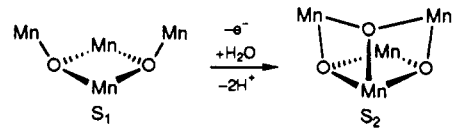

(5)

of a μ_3-Cl^- bridging Mn1, Mn1′, and Mn1″). This transformation requires relatively little structural change to the Mn_4O_2 core. Note that the lower $[Mn_2(\mu\text{-}O)_2]$ rhomb is present in both **2** and **6** with little change in metric parameters. The major change required is approach of the two "wing-tip" Mn atoms of the butterfly to occupy positions Mn(1) and Mn(1′) of **2**. These manganese ions are ca. 5.6 Å apart in **6** (and **7**) and ca. 3.3 Å apart in **2**. The approach of the two manganese ions is accomplished by an increase in the pyramidality of the μ_3-O^{2-} groups; the sum-of-angles at the bridging oxides is ca. 350° in **6** but only ca. 305° in **2**. As a result, the μ_3-oxides are ca. 0.33 Å above their Mn_3 planes in **6** and ca. 0.84 Å in **2**. Similarly, the dihedral angle between the two Mn_3 planes in **6** is ca. 135° but only ca. 104° in **2**. Thus, the "addition" of a third bridging oxide to the Mn_4O_2 core causes a closing-up to form the Mn_4O_3 core, the change required being only a decrease in the wing-tip Mn···Mn separation by ca. 2.3 Å by "pivoting" of the wing-tip Mn–O bond about the briding oxides, with very little change to the central Mn_2O_2 rhomb. We thus feel it valid to propose for consideration the possibility that $[Mn_4O_2]^{8+}$ and $[Mn_4O_3Cl]^{6+}$ structural units may be present at S_1 and S_2, respectively.

It should, of course, be remembered that in the absence of structural data on the WOC, it is unclear to what degree the synthetic complexes reproduce the precise structural features of the native Mn_4 site. Nevertheless, the synthesized materials are capable, at the very least, of providing insights into the type of chemistry and structural changes that might be occurring during the catalytic cycle. In particular, the increase in oxide content during S_n state (oxidation state) advancement, as suggested by potential models **6** (S_1) and **2** (S_2) provides interesting food for thought. In fact, the inorganic chemistry we are unearthing leads us to suspect that at the heart of the WOC mechanism may lie a coupling of sequential oxidation state increase (S_n state advancement) with sequential substrate (H_2O) incorporation into the Mn_4 aggregate. As briefly described elsewhere,[26] this coupling of the two processes could have a dual purpose. Firstly, the increasing average Mn_4 oxidation level would be stabilized by an increase in the number of "hard" oxide bridging ligands and this facilitates subsequent further oxidation; note that the WOC is oxidized by P680+, the cation radical generated by charge separation at photosystem II, via intermediacy of tyrosine radical Z^+, so that the oxidation potential for each S_n/S_{n+1} couple must remain within the capability of Z^+ (~0.9–1.0 V vs NHE).[12] Secondly, the sequential incorporation and deprotonation (the displaced bridging carboxylates could act as H^+ acceptors) of H_2O molecules *into* the Mn_4 aggregate is a means by which the substrate is activated for subsequent oxidation to O_2. In addition, the conversion of H_2O groups into bridging oxides brings them into closer spatial proximity (ca. 2.5 Å in **6** and **2**) again facilitating subsequent O–O bond formation. Thus, there may be a synergistic relationship between the Mn_4 aggregate (deprotonation, activation, and oxidation of substrate) and its H_2O substrate (control of Mn_4 oxidation potential to facilitate S_n state advancement). If these ideas are valid, the S_3 state would be suggested to involve an Mn_4O_4 core, as shown in eq 6. The precise structure of such an Mn_4O_4 unit is difficult to predict, but an Mn_4O_4 cubane is one possibility.[40]

(39) (a) Vincent, J. B.; Christou, G. *Inorg. Chim. Acta* **1987**, *136*, L41. (b) Vincent, J. B.; Christou, G. *Biochim. Biophys. Acta* **1988**, *895*, 259.

$$\underset{S_1}{Mn_4O_2} \xrightarrow[-e^-,\ +Cl^-]{+H_2O} \underset{S_2}{Mn_4O_3Cl} \xrightarrow[-e^-]{+H_2O} \underset{S_3}{Mn_4O_4} \qquad (6)$$

In support of the above ideas, note that the coupling of increasing oxidation state and oxide content was first demonstrated by Wieghardt and co-workers[41a] who achieved the conversion of $[Mn_2O(O_2CCH_3)_2L_2]^{2+}$ ($2Mn^{III}$) to $[Mn_2O_2(OAc)L_2]^{2+}$ (Mn^{III}, Mn^{IV}) where L = 1,4,7-triazacyclononane. The same group has since reported[41b] the final member of this series, $[Mn_2O_3L_2]^{2+}$ ($2Mn^{IV}$), with three bridging oxides. More recently, we demonstrated the conversion of the Mn_4O_2 complex $[Mn_4O_2(OAc)_6(py)_2(dbm)_2]$ to the Mn_4O_3Cl complex $[Mn_4O_3Cl(OAc)_3(dbm)_3]$ (dbmH = dibenzoylmethane).[25]

Finally, the presence of the μ_3-Cl^- in the Mn_4O_3Cl complexes is intriguing, remembering the Cl^- dependence for activity of the WOC. In the absence of Cl^-, the WOC forms an abnormal S_2 state and O_2 evolution is blocked.[42] The precise role of Cl^- is currently unclear, but the present results do establish a precedence in Mn_4 chemistry for the possibility that it may be required as a bridging ligand at some S_n states. We have been unable to date to obtain Mn_4 complexes at the $3Mn^{III}$, Mn^{IV} level that do not contain Cl^-, and attempts to remove the Cl^- ions from $[Mn_4O_3Cl]^{6+}$ cubanes (for example, with Ag^+ sources) have resulted only in cluster degradation. Since the bridging Mn–Cl bond distances are long (>2.6 Å), it is also unclear to what extent current EXAFS conclusions[38] about the number of ca. 2.7 Å Mn···Mn separations in the WOC may be affected by the presence of bridging Cl^- ions (vide infra).

Infrared Spectroscopy. The availability of complexes **1**, **2**, **4**, and **5**, and their near-superimposable $[Mn_4O_3Cl]^{6+}$ cores, allows comparisons between IR spectra. The goal is to identify bands that are diagnostic of this type of Mn_4 aggregate and that would be useful as a diagnostic tool for future examples without recourse to crystallography. The spectra of the four complexes show several common bands that are essentially invariant in position and appearance. These are collected in Table III. The ν_{as} (COO) stretches are in the 1540–1560-cm^{-1} range and are low compared to those for carboxylates bridging Mn^{III} centers [$\sim$1600 cm^{-1} in $[Mn_3O(O_2CMe)_6(py)_3](ClO_4)$, for example]. More diagnostic for $[Mn_4O_3Cl]$ complexes, however, are the bands in the Mn–O stretching region of the spectrum (400–700 cm^{-1}), particularly the strong band at 580–590 cm^{-1}, which is a region that rarely contains any features in the spectra of the many other Mn/O/RCO_2^- aggregates that we have investigated. This suggests this band arises from the $[Mn_4O_3Cl]^{6+}$ core. These IR features have recently proven their worth in providing early indications of the unexpected formation of the $[Mn_4O_3Cl]^{6+}$-containing product $[Mn_4O_3Cl_4(O_2CCH_3)_3(dbm)_3]$ (dbmH = dibenzoylmethane) from the reaction of $[Mn_4O_2(O_2CCH_3)_6(py)_2(dbm)_2]$ with Cl^-.[25]

Electrochemistry and Reactivity Studies. An electrochemical study of complex **2** in CH_2Cl_2 using cyclic voltammetry displayed no reversible features. Only very broad waves indicating irreversible processes were detected in both anodic and cathodic scans, showing the complex to be very unstable at other oxidation levels. This is in stark contrast to the $[Mn_4O_2]$ butterfly complexes which display reversible features and which have been isolated in three oxidation levels.[26,31]

Ligand substitution of bound $CH_3CO_2^-$ groups by $PhCO_2^-$ upon addition of excess PhCOOH to polynuclear oxo–acetate complexes has been demonstrated for $[Mn_4O_2]^{8+}$ complexes,[26,31] and it had been hoped that a similar reaction of complex **2** might yield unknown $[Mn_4O_3Cl_4(O_2CPh)_3(py)_3]$, which would have improved solubility. However, treatment of **2** with 3 or more equiv of PhCOOH led only to mixtures of products that have proven difficult to separate for characterization. It appears that the $[Mn_4O_3Cl]$ core does not retain its structural integrity under these conditions.

Disruption of the $[Mn_4O_3Cl]^{6+}$ core of **2** also resulted on treatment of **2** with bpy. Addition of 4–8 equiv of bpy to **2** in CH_2Cl_2 led to slow precipitation of microcrystals of $[Mn_2O_2(OAc)Cl_2(bpy)_2]$, identified by IR comparisons with an authentic sample.[43] The optimum yield of the $Mn^{III}Mn^{IV}$ complex was 40% (based on Mn) after a three-day reaction period with 6 equiv of bpy. This result was not unanticipated, for our original synthesis of the dinuclear complex involved addition of bpy to the complex **2** reaction solution prior to crystallization of the cubane complex.[43]

Proton NMR Spectroscopy. An NMR investigation of the $[Mn_4O_3Cl]^{6+}$-containing complexes has been carried out in order to probe their solution behavior and complement that previously reported for the $[Mn_4O_2]^{8+}$ butterfly complexes.[26,31] The low solubility of the present complexes has hampered these results, a problem not encountered with the $[Mn_4O_2]^{8+}$ complexes for which both solvent variations and temperature-dependence studies were possible. Studies have consequently been restricted to complexes **2** and **4** in CD_2Cl_2 and $CDCl_3$. The complexes have a large magnetic moment at room temperature ($\sim$8.7 μ_B), and the proton resonances are thus very broad and shifted from their diamagnetic resonance positions. The C_3 symmetry observed in the solid-state structure should result in a total of four ligand resonances, one from the symmetry equivalent $CH_3CO_2^-$ groups, and three from the three equivalent py groups (ortho, meta, and para protons). In CD_2Cl_2 and $CDCl_3$, three broad resonances could clearly be seen at 43.9, −3.2, and −52.3 ppm. To assist in assignments recourse was made to deuterated derivatives, viz., $[Mn_4O_3Cl_4(O_2CCD_3)_3(py)_3]$ (**2a**) and $[Mn_4O_3Cl_4(OAc)_3(C_5D_5N)_3]$ (**2b**), prepared by utilizing the appropriate deuterated reagents in the procedure for complex **2**. The data obtained from these three complexes are listed in Table IV. The spectrum for **2a** clearly identifies the 43.9 ppm resonance as due to the $CH_3CO_2^-$ protons, since this (and only this) peak is absent. The −3.2 and −52.3 ppm peaks are therefore assigned as py resonances. This is supported by the spectrum of complex **2b**, which displays the 43.9 ppm resonance but not those at −3.2 and −52.3 ppm. The latter in the spectra of **2** and **2a** have relative areas of 2:1, respectively, identifying the −52.3 ppm peak as due to the para protons. The −3.2 ppm peak is consequently assigned to the meta protons. The question arises as to the whereabouts of the resonance for the ortho protons. These are the closest to the paramagnetic centers (<3 Å in the solid-state structure) and would be expected to experience the greatest relaxation broadening amongst the ligand resonances. Within the constraints of the limited solubility, numerous attempts were made to detect the ortho proton resonance, including varying spectral acquisition parameters, but all to no avail, and we conclude that it is broadened beyond detection.

The ^2H NMR spectra of complexes **2a** and **2b** were also obtained, to both further confirm the assignments of the detected resonances and possibly locate the ortho resonance. The data are included in Table IV. The ^2H NMR spectrum of **2a** contains only a peak at 43.8 ppm confirming this as the $CH_3CO_2^-$ resonance, whereas the spectrum of **2b** displays the two py resonances at −3.4 and −51.6 ppm.

The observation of spectra consistent with the solid-state structure supports retention of the C_3 symmetry structure on dissolution in these solvents. We see no other resonances except for solvent impurities and MeCN of crystallization. Retention of the solid-state structure in solution is also supported by rigorous adherence by complex **2** to Beer's law in CH_2Cl_2 in the concentration range 0.11–1.11 mM. Complex **4**, which is sufficiently soluble in MeCN, also obeys Beer's law in this stronger donor solvent in the concentration range 0.05–0.40 mM. Complex **1** is insoluble in CH_2Cl_2 or CH_3CN, but it dissolves in DMF; in the latter solvent it rigorously obeys Beer's law in the concentration

(40) At higher ($\geq Mn^{III}$) oxidation levels such cubanes are not known in discrete form although they are found as the central portion of $[Mn_{12}O_{12}(O_2CR)_{16}(H_2O)_4]$ (R = Me, Ph). See: (a) Lis, T. *Acta Crystallogr., Sect. B* **1980**, *B36*, 2042. (b) Boyd, P. D. W.; Li, Q.; Vincent, J. B.; Folting, K.; Chang, H.-R.; Strieb, W. E.; Huffman, J. C.; Christou, G.; Hendrickson, D. N. *J. Am. Chem. Soc.* **1988**, *110*, 8537.

(41) (a) Wieghardt, K.; Bossek, U.; Zsolnai, L.; Huttner, G.; Blondin, G.; Girerd, J.-J.; Babonneau, F. *J. Chem. Soc., Chem. Commun.* **1987**, 651. (b) Wieghardt, K.; Bossek, U.; Nuber, B.; Weiss, J.; Bonvoisin, J.; Corbella, M.; Vitols, S. E.; Girerd, J.-J. *J. Am. Chem. Soc.* **1988**, *110*, 7398.

(42) (a) Izawa, S.; Heath, R. L.; Hind, G. *Biochim. Biophys. Acta* **1969**, *180*, 388–398. (b) Kelley, P. M.; Izawa, S. *Biochim. Biophys. Acta* **1978**, *502*, 198–210.

Table IV. Proton NMR Data for Complexes **2** and **4** in CD_2Cl_2[a]

complex	nucleus	O_2CR	py
2	^1H	43.9	−3.2 (m), −52.3 (p)
2a[b]	^1H		−3.2 (m), −52.3 (p)
2b[c]	^1H	43.9	
2a	^2H	43.8	
2b	^2H		−3.4 (m)
			−51.6 (p)
4	^1H	25.7, 40.0 (CH_2)	−3.5 (m)
		10.2 (CH_3)	−52.6 (p)
4a	^1H	25.7, 40.0 (CH_2),	
		10.2 (CH_3)	

[a] Chemical shifts are in ppm vs TMS at ~25 °C. Chemical shifts in $CDCl_3$ solution are essentially the same. [b] Complex **2a** is $[Mn_4O_3Cl_4(O_2CD_3)_3(py)_3]$. [c] Complex **2b** is $[Mn_4O_3Cl_4(OAc)_3(C_5D_5N)_3]$. [d] Complex **4a** is $[Mn_4O_3Cl_4(O_2CCH_2CH_3)_3(C_5D_5N)_3]$.

range 0.020–0.10 mM. Similar conclusions were reached for the $[Mn_4O_2]^{8+}$ complexes.[26,31] It thus appears that these examples of oxide-bridged Mn_4 complexes are capable of retaining their structural integrity on dissolution.

The ^1H NMR spectrum of complex **4** displays two peaks at −52.6 and −3.5 ppm assignable to the py para and meta protons (Table IV). There are now, however, a total of three peaks in the downfield region of the spectrum, at 40.0, 25.7, and 10.2 ppm in an approximate ratio of 1:1:3. The latter is assigned to the propionate CH_3 protons, whereas the former two, which have the same broadness, are assigned to the diastereotopic protons of the propionate CH_2 group. The spectrum of the deuterated pyridine version **4a**, prepared in a similar fashion as **4**, showed the absence of only the upfield resonances, ruling out any of the downfield resonance to be from the py ortho proton.

Magnetochemistry: Variable-Temperature Magnetic Susceptibility Studies. Plots of effective magnetic moment per molecule versus temperature for complexes **1**, **2**, and **4** measured at 10.0 kG are shown in Figure 3. For all three complexes the effective magnetic moment increases as the temperature is decreased from room temperature until a maximum in μ_{eff} is found. The maximum effective moments per molecule occur at 60, 60, and 15 K with effective moments of 9.54, 9.28, and 9.97 μ_B for complexes **1**, **2**, and **4**, respectively. A further decrease in temperature below the temperature of maximum μ_{eff} leads to a decrease in the effective moment. For complex **4** there is a plateau at a moment of ~9.9 μ_B that spans the temperature range 60–15 K, below which a sharp decrease in μ_{eff} occurs. The effective moments at 300, 302, and 320 K are 8.82, 8.65, and 9.09 μ_B for complexes **1**, **2**, and **4**, respectively.

If there were no exchange interactions between the metal ions in a $Mn^{IV}Mn_3^{III}$ complex, the spin-only effective magnetic moment would be 9.33 μ_B, and it would be independent of temperature. Clearly there are appreciable magnetic exchange interactions between the manganese ions in complexes **1**, **2**, and **4**. For an $S = {}^9/_2$ spin state, the spin-only effective moment would be 9.94 μ_B. The plateau value of μ_{eff} observed for **4** comes very close to this value, while those for complexes **1** and **2** fall short. The decrease in μ_{eff} at low temperature may be attributed to some combination of factors such as saturation of the lowest M_s component of the Zeeman split Kramers doublet comprising the ground state, zero-field splitting (ZFS) of the ground state, and intercluster magnetic exchange interactions. These will be addressed in the next section.

In order to assess the distribution of spin states and nature of the exchange interactions in complexes **1**, **2**, and **4** a Heisenberg–Dirac–van Vleck (HDVV) spin Hamiltonian $(-2J\hat{S}_i\cdot\hat{S}_j)$ for pairwise exchange interactions was employed. The spin Hamiltonian for a $Mn^{IV}Mn_3^{III}$ complex with C_3 symmetry is given by eq 7

$$\hat{\mathcal{H}} = -2J_{33}(\hat{S}_1\cdot\hat{S}_2 + \hat{S}_1\cdot\hat{S}_3 + \hat{S}_2\cdot\hat{S}_3) - 2J_{34}(\hat{S}_1\cdot\hat{S}_4 + \hat{S}_2\cdot\hat{S}_4 + \hat{S}_3\cdot\hat{S}_4) \quad (7)$$

where $S_1 = S_2 = S_3 = 2$ and $S_4 = {}^3/_2$. In order to solve this Hamiltonian for the appropriate eigenvalue expression, the Kambe vector coupling method[44] was used. The spins of the three Mn^{III} ions are vectorially coupled together to give $\hat{S}_A$ $(=\hat{S}_1 + \hat{S}_2 + \hat{S}_3)$ and then $\hat{S}_A$ is vectorially coupled to the Mn^{IV} spin $\hat{S}_4$ to give the total spin $\hat{S}_T$ $(=\hat{S}_A + \hat{S}_4)$. By an operator replacement technique eq 7 can be changed to a form involving only $\hat{S}^2$ operators from which it is easy to write eq 8 which gives the eigenvalues for all states. The total degeneracy for a $Mn^{IV}Mn_3^{III}$ complex is 500.

$$E(S_T, S_A) = -J_{34}[S_T(S_T + 1) - S_A(S_A + 1)] - J_{33}[S_A(S_A + 1)] \quad (8)$$

There are 24 different spin states, where S_A varies from 0 to 6 in integers and S_T varies from ${}^1/_2$ to ${}^{15}/_2$ in integers. Substitution of these energies into the Van Vleck equation[30] gives a theoretical expression for the molar susceptibility of a C_3 symmetry $Mn^{IV}Mn_3^{III}$ complex. This was generated in a computer program. There are three parameters: an average g for the Zeeman interaction, J_{33} which gauges the $Mn^{III}\cdots Mn^{III}$ interaction, and J_{34} which gauges the $Mn^{III}\cdots Mn^{IV}$ interaction.

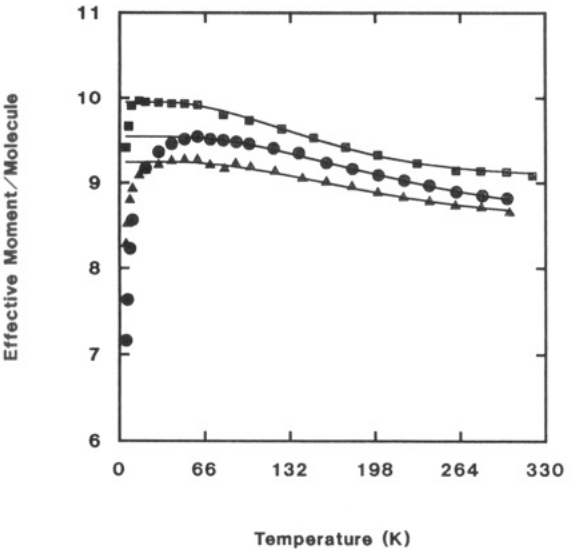

Figure 3. Plots of effective magnetic moment (μ_{eff}) per molecule versus temperature for three $Mn^{IV}Mn_3^{III}O_3Cl$ complexes: ○, $(H_2Im)_2[Mn_4O_3Cl_6(O_2CCH_3)_3(HIm)]\cdot{}^3/_2CH_3CN$ (**1**); △, $[Mn_4O_3Cl_4(O_2CCH_3)_3(py)_3]\cdot{}^3/_2CH_3CN$ (**2**); and □, $[Mn_4O_3Cl_4(O_2CCH_2CH_3)_3(py)_3]\cdot{}^5/_2CH_3CN$ (**4**). The solid lines result from fitting the data to the theoretical model. See the text for the fitting parameters.

It should be noted that unlike complexes **2** and **4**, complex **1** is not rigorously of C_3 symmetry. The Mn_4O_3Cl core of complex **1** is, however, essentially superimposable with the cores of complexes **2** and **4**. Since it is likely that the three μ_3-O^{2-} and the one μ_3-Cl^- provide the primary magnetic exchange pathways for the interactions, the use of the above model is reasonable and provides a consistent means of comparison for the three complexes. The solid lines in Figure 3 represent the best fits of the experimental data to the theoretical susceptibility equation. The data for complex **1** were fit down to 40.0 K, those for complex **2** down to 15.0 K, and those for complex **4** down to 39.99 K. All data are available in the supplementary material. It is important to note that the theoretical fits shown in Figure 3 are plotted to 5.0 K. The values of g, J_{33}, and J_{34} determined by these fits are given in Table V. The exchange parameter J_{33} is ferromagnetic and ranges from 8.58 to 11.3 cm^{-1}, while J_{34} is antiferromagnetic and ranges from −30.3 to −20.8 cm^{-1}. For each complex, the ground state is a $S_T = {}^9/_2$ $(S_A = 6)$ state, where the lowest energy excited states have $S_T = {}^7/_2$ $(S_A = 5)$ and $S_T = {}^{11}/_2$ $(S_A = 6)$. The energy separations of these two excited states relative to the ground state are also given in Table V. It is clear that the $S = {}^9/_2$ ground state is well isolated.

In a previous communication[24] on complex **2**, it was reported that an exhaustive search of parameter space produced three possible fits, each representing local minima in the residual error surface. The best fit was chosen based upon detailed high field magnetization studies[24] which showed that the $S = {}^9/_2$ ground

Table V. Parameters Obtained from Fitting the 10 kG Susceptibility Data of $(H_2Im)_2[Mn_4O_3Cl_6(O_2CCH_3)_3]\cdot CH_3CN$ (1), $[Mn_4O_3Cl_4(O_2CCH_3)_3(C_5H_5N)_3]\cdot 4CH_3CN$ (2), and $[Mn_4O_3Cl_4(O_2CCH_3CH_2)_3(C_5H_5N)_3]\cdot 4CH_3CN$ (4)[a]

parameter/complex	1	2	4
g	1.92	1.86	2.00
J_{34} (cm^{-1})	-30.3	-23.1	-20.8
J_{33} (cm^{-1})	11.1	11.3	8.6
$E(^7/_2)$ (cm^{-1})	223.7	205.4	165.4
$E(^{11}/_2)$ (cm^{-1})	333.3	254.0	229.0

[a] The energies of the two lowest energy excited states are also given.

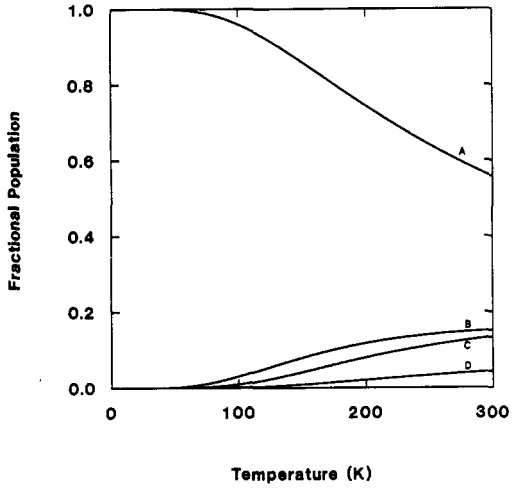

Figure 4. Plots of fractional populations of the $S_T = {}^9/_2$ ground state and low-lying excited states versus temperature for $(H_2Im)_2[Mn_4O_3Cl_6(O_2CCH_3)_3(HIm)]\cdot{}^3/_2CH_3CN$ (1). The code is A ($S_T = {}^9/_2$ state), B ($^7/_2$), C ($^{11}/_2$), and D ($^5/_2$).

state was well isolated for complex 2. For two of the three minima an isolated $S = {}^9/_2$ state was *not* found, and these two fits were therefore deemed unreasonable. For complexes 1 and 4, similar sets of three minima were found. Upon the basis of the arguments presented for complex 2 we have also decided that the best fit of the data for complexes 1 and 4 (vide infra) is the one which gives an isolated $S_T = {}^9/_2$ ground state. The values of J_{33} and J_{34} reported in this paper are slightly different from those previously reported[24] for complex 2. This is due to noise in the experimental data near 80 K which results in noise in the residual error surface.

The observed gradual decrease in effective moment at higher temperatures for complexes 1, 2, and 4 results from thermal population of the $S_T = {}^7/_2$ excited state. While the largest separation between ground state and excited states is found for complex 1, complex 4 has the smallest separation. Plots of population versus temperature for the $S_T = {}^9/_2$ ground state and several low-lying excited states for complex 1 are given in Figure 4. Differences in the shapes of the magnetic moment versus temperature profiles result from these variations in spin-state populations. In both cases, the initial decrease in μ_{eff} results from population of the $S_T = {}^7/_2$ state. For complex 4, however, this decline in μ_{eff} is mitigated by the fact that the $S_T = {}^{11}/_2$ state is also being populated. In fact, at higher temperatures the population of the $S_T = {}^{11}/_2$ state exceeds that of the $S_T = {}^7/_2$ state due to differences in their degeneracies.

The results of recent studies[31,45] of magnetic exchange interactions in polynuclear complexes have pointed to the need to determine how well the exchange parameters are known. Just how well J_{34} and J_{33} are determined for a $Mn^{IV}Mn_3^{III}$ complex can be addressed by carefully examining the residual error of

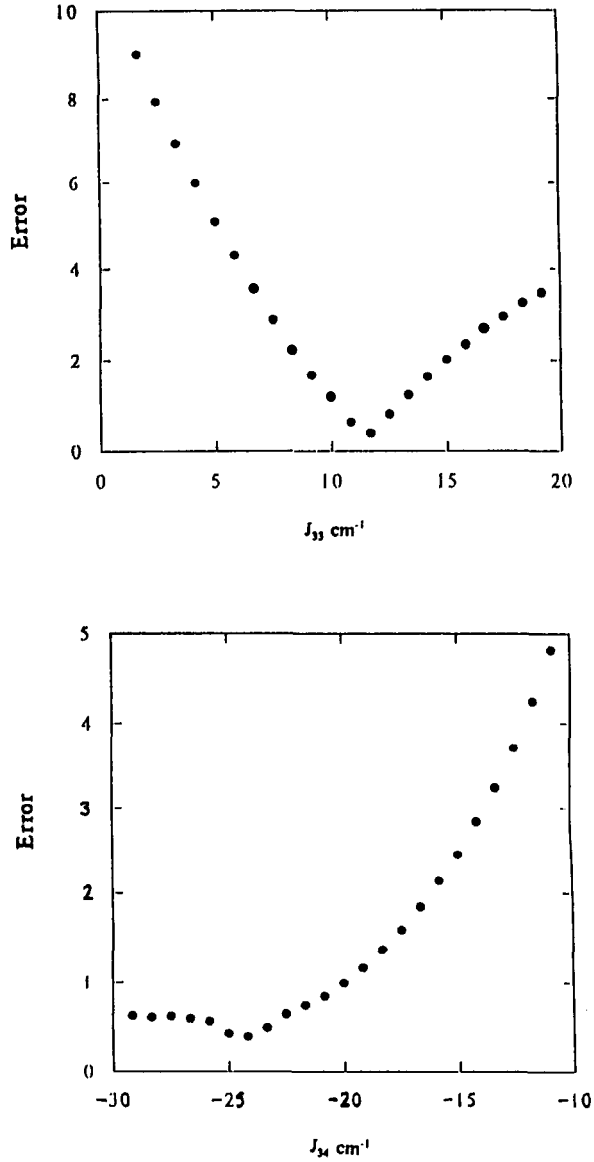

Figure 5. Plots of the residual error of fitting, E_r, versus the exchange parameter J_{33} and E_r versus J_{34} are shown for $[Mn_4O_3Cl_4(O_2CCH_3)_3(py)_3]\cdot{}^5/_2CH_3CN$ (4). In the case of the E_r versus J_{33} plot the values of J_{34} and g were held fixed at the best fit values. For the E_4 versus J_{34} plot the values of J_{33} and g were held fixed.

fitting, E_r, as a function of the J_{33} and J_{34} parameters, where E_r is defined in eq 9:

$$E_r = \frac{100 \sum_i [\mu_{eff}^i(\text{exp}) - \mu_{eff}^i(\text{calc})] w_i}{\sum_i \mu_{eff}^i(\text{exp})} \quad (9)$$

In eq 9 w_i is a weighting factor. Plots of E_r as a function of either J_{33} or J_{34} for complex 4 are shown in Figure 5. There is a sharp minimum in E_r versus J_{33}, which indicates that J_{33} is well determined. On the other hand, the minimum in E_r versus J_{34} is less well determined, particularly for more negative antiferromagnetic values of J_{34}. This trend was also found for the other two complexes. The reason for these relative sensitivities in fitting for J_{33} and J_{34} basically reflect the fact that the $S_T = {}^9/_2$ state is well isolated from the excited states. The energies of the $S_T = {}^7/_2$ ($S_A = 5$) and $S_T = {}^{11}/_2$ ($S_A = 6$) lowest energy excited states relative to the $S_T = {}^9/_2$ ($S_A = 6$) ground state are given by eq 10. Since the energy of the lowest excited state ($S_T = {}^7/_2$) is four times more dependent upon J_{33} and J_{34}, the value of J_{33} is better

$$\Delta E(S_T = {}^7/_2) = -3.0J_{34} - 12.0J_{33} \quad (10)$$

$$\Delta E(S_T = {}^{11}/_2) = -11.0J_{34}$$

(43) Bashkin, J. S.; Schake, A. R.; Vincent, J. B.; Huffman, J. C.; Christou, G.; Chang, H.-R.; Li, Q.; Hendrickson, D. N. *J. Chem. Soc., Chem. Commun.* **1988**, 700–702.
(44) Kambe, K. *J. Phys. Soc. Jpn.* **1950**, *5*, 48.
(45) McCusker, J. K.; Vincent, J. B.; Schmitt, E. A.; Mino, M. L.; Shin, K.; Coggin, D. K.; Hagen, P. M.; Huffman, J. C.; Christou, G.; Hendrickson, D. N. *J. Am. Chem. Soc.* **1991**, *113*, 3012–3021.

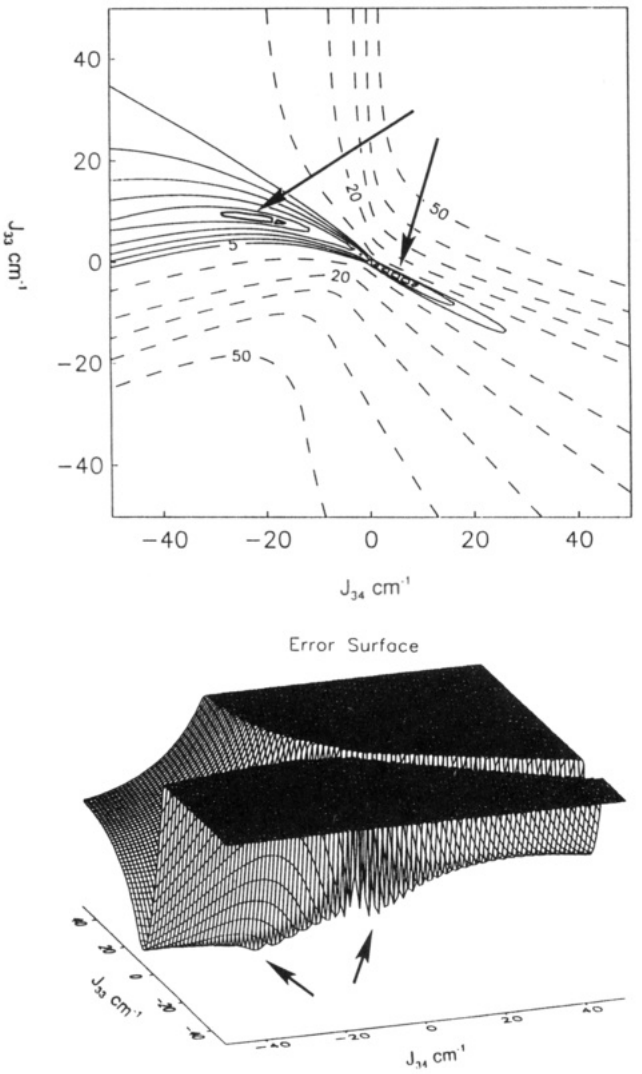

Figure 6. Surface and contour plots of residual error of fitting, E_r, as a function of J_{33} and J_{34} showing local fitting minima for $[Mn_4O_3Cl_4(O_2CCH_2CH_3)_3(py)_3]\cdot{}^5/_2CH_3CN$ (**4**). The surface plot is clipped at a E_r value of 10%.

determined. Unlike the $S_T = {}^7/_2$ state, the relative energy of the $S_T = {}^{11}/_2$ state is dependent only upon J_{34}. Thus, for this region of parameter space the ability to determine J_{34} is limited by the low thermal population of the $S_T = {}^{11}/_2$ state. The estimated uncertainty in J_{33} is of the order of 5% and that for J_{34} is of the order of 10%.

It is also informative to examine the residual error surface as a function of J_{33} and J_{34} to see the interrelationship of different fitting minima and the correlation between these two parameters. Surface and contour plots of E_r as a function of J_{33} and J_{34} are shown in Figure 6 for complex **4**. Two local minima in E_r are in evidence in the region where both J_{33} and J_{34} are allowed to vary from +40 to −40 cm^{-1}. Similar plots have been found for the other two complexes. One minimum, believed to be the global minimum, corresponds to the best fit described above where there is a well-isolated $S = {}^9/_2$ ground state, $J_{33} = 8.6$ and $J_{34} = -21$ cm^{-1}. The other minimum occurs where $J_{33} = -3.6$ cm^{-1} and $J_{34} = +7.4$ cm^{-1}. As described above, this second minimum was discounted for it corresponds to an $S_T = {}^9/_2$ ground state with an $S_T = {}^7/_2$ excited state separated by only 0.5 cm^{-1} and seven other spin states lying within 50 cm^{-1} of the ground state. From the surface plot it is evident that this second minimum has a greater relative error associated with it. Furthermore, this second minimum can be discounted because there is no reported case of a ferromagnetic Mn^{IV}–Mn^{III} magnetic exchange interaction.

Since these $Mn^{IV}Mn_3^{III}$ complexes have been prepared to model the S_2 state of the water oxidation center of photosystem II, it

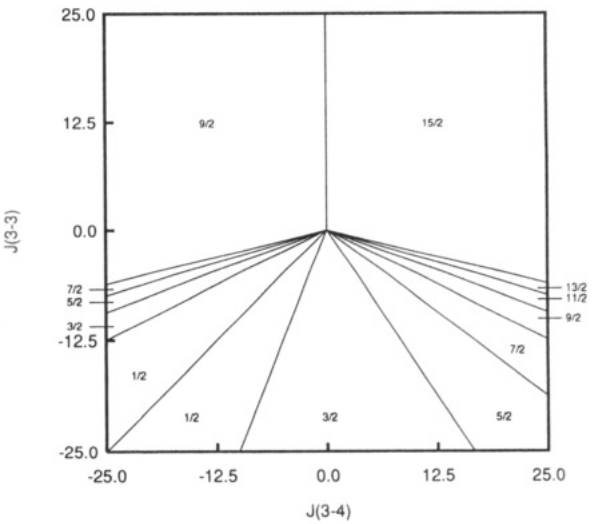

Figure 7. Map in the J_{33}–J_{34} parameter space of which state is the ground state for a cubane $Mn^{IV}Mn_3^{III}$ complex. Each region of this parameter space is labeled with the spin (S_T) of the ground state.

is important to understand the origin of the $S_T = {}^9/_2$ ground state. The S_2 state has been reported[14] to have a $S_T = {}^1/_2$ ground state, so it is also important to discover what changes in the present $Mn^{IV}Mn_3^{III}$ complexes are necessary in order to get a $S_T = {}^1/_2$ ground state. For a $Mn^{IV}Mn_3^{III}$ complex with C_3 symmetry it is theoretically possible to have a ground state with a spin in the range from $S_T = {}^{15}/_2$ to $S_T = {}^1/_2$ in integers. From a mathematical point of view the relative energy of each spin state is a function of J_{33} and J_{34} in accord with eq 8. Substitution of the appropriate values for S_T and S_A into eq 8 produces a set of 24 equations describing the energies of the 24 different states. Various values of J_{33} and J_{34} can be put into these equations and the ground state evaluated. This was done for a large part of (J_{33},J_{34}) parameter space.

Figure 7 summarizes which state is the ground state for values of J_{33} and J_{34} in the range of +25 to −25 cm^{-1} when the external magnetic field is zero. At the origin of this diagram where $J_{33} = J_{34} = 0$ all 24 states are energetically degenerate as per eq 8. When either of these parameters is nonzero, then one state is the ground state. There are only 13 states which can be the ground state. Since all $Mn^{IV}\cdots Mn^{III}$ interactions have been reported (vide infra) to be antiferromagnetic, we should consider the left side of the diagram where $J_{34} < 0$. There are seven states which are candidates for the ground state when $J_{34} < 0$. If the spins on the three Mn^{III} ions are ferromagnetically aligned, then $S_A = 6$. In this case the ground state has $S_T = {}^9/_2$ due to the antiferromagnetic coupling of $S_A = 6$ and $S_4 = {}^3/_2$ (Mn^{IV} ion). If the J_{33} interaction is antiferromagnetic and $|J_{33}| > 0.25\,|J_{34}|$, then $S_A = 5$ and the ground state has $S_T = {}^7/_2$. In fact, if $J_{34} < 0$ and if J_{34} is kept constant, then as J_{33} becomes more and more negative the value of S_A decreases from 6 to 0 in integer values. This leads to S_T varying consecutively through ${}^9/_2$, ${}^7/_2$, ${}^5/_2$, ${}^3/_2$, ${}^1/_2$ ($S_A = 2$) and ${}^1/_2$ ($S_A = 1$) to finally give $S_T = {}^3/_2$ ($S_A = 0$). In this series there is spin frustration. This term refers to an effect whereby the interplay of various exchange pathways in a complex results in spin vector alignments which deviate from those anticipated based upon the intrinsic nature of the pairwise exchange interactions.

The relative magnitudes of the pairwise exchange interactions in a $Mn^{IV}Mn_3^{III}$ complex determine which ground state is present. If both J_{33} and J_{34} are negative and $|J_{33}| \gg |J_{34}|$, then the J_{33} interactions dominate the J_{34} interactions and all the Mn^{III} ions pair up to give $S_A = 0$. In this case the Mn^{IV} ion ($S_4 = {}^3/_2$) can be described as being frustrated; it cannot pair up with the Mn^{III} ions. If J_{33} and J_{34} become comparable in magnitude, then the three Mn^{III} ions cannot pair up completely and S_A takes a value between 1 and 5. An increase in the dominance of the J_{34} interaction decreases the value of S_A. Eventually, the J_{34} is totally dominating and this frustrates the $Mn^{III}\cdots Mn^{III}$ interactions so

that they cannot pair up and this gives $S_A = 6$.

Spin frustration is not a new concept, for it has been shown to be the origin of several interesting phenomena detected for extended magnetic exchange interacting compounds.[46] For example, even though the solid-state structure of $CsCoCl_3$ shows a one-dimensional chain structure formed by face-sharing $CoCl_6^{4-}$ octahedra, neutron diffraction experiments[47] show that due to interchain magnetic exchange interactions the chains of $CsCoCl_3$ form a triangular lattice and interact antiferromagnetically. The spin frustration among the magnetic chains results in phase transitions at $T_{N1} = 21.5$ and $T_{N2} = 9.2$ K. Spin frustrated exchange interacting complexes have attracted considerable attention in recent years due to unusual lattice dynamics phenomena[48] and the possibility of new types of phase transitions.[49]

The concept of spin frustration in molecular species is relatively new.[50] Triangular trinuclear complexes exhibit spin frustration which is easily understood by reference to a hypothetical triangular Cu_3^{II} complex. Antiferromagnetic pairwise exchange interactions

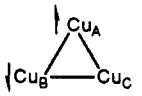

are commonplace. If there is a strong antiferromagnetic interaction between the Cu_A and Cu_B ions, then the spin on the Cu_C ion is frustrated and remains unpaired. There are other topological arrangements of polynuclear complexes which can exhibit spin frustration. Very recently we reported spin frustration in Fe_4^{III} complexes[45] and Mn_4^{III} complexes[31] with a butterfly construction, viz. For the Mn_4^{III} complexes the ground state has $S_T = 3$. This

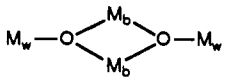

results from a body–body ($M_b \cdots M_b$) interaction which is more antiferromagnetic than and dominates the wing-body ($M_w \cdots M_b$) interaction. The two body Mn^{III} ions almost pair their spins, and this frustrates the spins on the two wing-tip Mn^{III} ions. Thus, one characteristic of a complex experiencing spin frustration is a ground state of intermediate spin, intermediate between the largest and smallest spin values possible. Very recently a Fe_6^{III} complex with an unusual $S_T = 5$ ground state was reported.[51] Two μ_3-oxide-bridged Fe_3^{III} triangles are bridged together by OH^- ions. Spin frustration in this hexanuclear ferric complex leads to an unusual $S = 5$ ground state.

In Table VI are collected exchange parameters for $Mn^{III} \cdots Mn^{III}$ and $Mn^{IV} \cdots Mn^{III}$ interactions in various polynuclear complexes with μ-oxide bridges. Binuclear complexes with $Mn^{IV}(\mu_3\text{-}O)_2Mn^{III}$ units exhibit strong antiferromagnetic interactions where J is in the range of -140 to -221 cm^{-1}. The Mn^{IV}–O–Mn^{III} bridge angles in these complexes are in the same range as those (Table II) observed for complexes **1**, **2**, and **4**, where the J_{34} values are -30.3, -23.1, and -20.8 cm^{-1}, respectively. The J_{34} interactions in complexes **1**, **2**, and **4** are probably less antiferromagnetic than in the binuclear complexes because the two $Mn^{IV} \cdots Mn^{III}$ bridges in the cubane complexes **1**, **2**, and **4** are μ_3-O^{2-} not μ_2-O^{2-} ions.

Table VI. Mn^{III}–Mn^{III} and Mn^{III}–Mn^{IV} Magnetic Exchange Parameters for Polynuclear Complexes[a]

complex	J (cm^{-1})	bridge
Mn^{III}–Mn^{III} Interactions		
$[Mn_4O_2(O_2CCH_3)_6(bipy)_2]$[b]	−3.12	$2\mu_3$-O
$[Mn_4O_2(O_2CCH_3)_7(bipy)_2](ClO_4)$[b]	−7.80	μ_3-O
	−23.53	$2\mu_3$-O
$[Mn_6O_2(O_2CPh)_{10}(py)_2(CH_3CN)_2]$[c]	−42.0	$2\mu_3$-O
$[Mn_9O_4(O_2CPh)_8(sal)_8(salH)_2(py)_4]$[d]	−26.2	$2\mu_3$-O
	−11.2	μ_3-O
$[Mn_3O(O_2CCH_3)_6(py)_3]\cdot py$[e]	−8.3	μ_3-O
$[Mn_2O(O_2CCH_3)_2(HB(pz)_3)_2]$[f]	−0.2 to −0.7	μ_2-O
$[LMnO]_2(ClO_4)_2\cdot H_2O$[g]	−86.4	$2\mu_2$-O
$[L'_2Mn_2O(O_2CCH_3)_2](ClO_4)_2$[h]	+9	μ_2-O
Mn^{III}–Mn^{IV} Interactions		
$[(bispicen)MnO]_2(ClO_4)_4\cdot 2CH_3CN$[i]	−140	$2\mu_2$-O
$[(L3)MnO]_2(ClO_4)_3$[j]	−176	$2\mu_2$-O
$[(L4)MnO]_2(ClO_4)_3$[j]	−221	$2\mu_2$-O
$[Mn_2O_2(bpy)_4](ClO_4)_3$[k]	−150	$2\mu_2$-O
$[Mn_2O_2(phen)_4](PF_6)_3$[l]	−148	$2\mu_2$-O

[a] Abbreviations: py = pyridine, bpy = bipy = bipyridine, salH2 = salicylic acid, $HB(pz)^{3-}$ = hydrotris(1-pyrazolyl)borate^{3-}, L = *N,N'*-bis((2-methylpyrid-2-yl)methyl)ethane-1,2-diamine, L' = 1,4,7-trimethyl-1,4,7-triazabicyclononane, L3 = ((6-methyl-2-pyridyl)methyl)(2-(2-pyridyl)ethyl)(2-pyridylmethyl)amine, L4 = ((6-methyl-2-pyridyl)methyl)bis(2-pyridylmethyl)amine, and phen = 1,10-phenanthroline. [b] Reference 26. [c] Schake, A. R.; Vincent, J. B.; Li, Q.; Boyd, P. D. W.; Folting, K.; Huffman, J. C.; Hendrickson, D. N.; Christou, G. *Inorg. Chem.* **1989**, *28*, 1915–1923. [d] Christmas, C.; Vincent, J. B.; Chang, H.-R.; Huffman, J. C.; Christou, G.; Hendrickson, D. N. *J. Am. Chem. Soc.* **1988**, *110*, 823. [e] Reference 27. [f] Sheats, J. E.; Czernuszewics, R. S.; Dismukes, G. C.; Rheingold, A. L.; Petrouleas, V.; Stubbe, J.; Armstrong, W. H.; Beer, R. H.; Lippard, S. J. *J. Am. Chem. Soc.* **1987**, *109*, 1435. [g] Goodson, P. A.; Oki, A. R.; Glerup, J.; Hodgson, D. J. *J. Am. Chem. Soc.* **1990**, *112*, 6248. [h] Oki, A. R.; Glerup, J.; Hodgson, D. J. *Inorg. Chem.* **1990**, *29*, 2435. [i] Goodson, P. A.; Glerup, J.; Hodgson, D. J.; Michelson, K.; Pedersen, E. *Inorg. Chem.* **1990**, *29*, 503. [j] Cooper, S. R.; Dismukes, G. C.; Klein, M. P.; Calvin, M. *J. Am. Chem. Soc.* **1978**, *100*, 7248. [k] Stebler, M.; Ludi, A.; Bürgi, H.-B. *Inorg. Chem.* **1986**, *25*, 4743–4750.

The third metal ion, a Mn^{III} ion interacting with each μ_3-O^{2-} ion in the

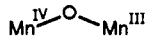

bridges of the complexes, functions as a Lewis acid. This Lewis acidity, in effect, removes some electron density from the oxide ion and the μ_3-O^{2-} ion is less effective in supporting an antiferromagnetic interaction compared to a μ_2-O^{2-} ion. Protonation of a μ_2-O^{2-} bridge to give a OH^- bridge similarly leads to a reduction in antiferromagnetic exchange interactions.[52]

The ferromagnetic $Mn^{III}(\mu\text{-}O)(\mu\text{-}Cl)Mn^{III}$ interaction in cubane complexes **1**, **2**, and **4** is characterized by J_{33} values in the +8.6 to +11.3 cm^{-1} range. Examination of Table VI shows that $Mn^{III}(\mu\text{-}O)_2Mn^{III}$ interactions with μ_2-O^{2-} ions vary from being moderately antiferromagnetic with $J_{33} = -86.4$ cm^{-1} to weakly antiferromagnetic with $J_{33} = -0.2$ to -0.7 cm^{-1}. Only two cases of ferromagnetic interactions between two oxo-bridged Mn^{III} ions are known, and in both cases the bridge between the Mn^{III} ions is of the (μ_2-O^{2-})bis(μ-carboxylate) type. For $[Mn_2O(O_2CPh)_2(bpy)_2(N_3)_2]$ (**8**) J_{33} was found to be +3.4 cm^{-1}, while for $[L_2Mn_2O(O_2CCH_3)_2](ClO_4)_2$ (**8**) a value of $J_{33} = +9$ cm^{-1} was given, where L is 1,4,7-trimethyl-1,4,7-triazacyclononane. A few $Mn^{III} \cdots Mn^{III}$ interactions propagated by μ_3-O^{2-} ions have been evaluated, see Table VI. All of these interactions are antiferromagnetic with J_{33} in the -3.1 to -42.0 cm^{-1} range. Thus, the ferrromagnetic $Mn^{III} \cdots Mn^{III}$ interactions in cubanes **1**, **2**, and **4** are somewhat unusual. The Mn^{III}–O–Mn^{III} bridge angle is 113.5–114.7°. For the two previously reported complexes which have ferromagnetic J_{33} interactions the bridge angles are 122.0° (complex **8**) and 120.9° (**9**). The Jahn–Teller elongated axis of

(46) See, for example: Tanaka, M.; Iwasaki, H.; Siratori, K.; Shindo, I. *J. Phys. Soc. Jpn.* **1989**, *58*, 1433 and references therein.

(47) Mekata, M.; Adachi, K. *J. Phys. Soc. Jpn.* **1978**, *44*, 806.

(48) Mekata, M.; Ajiro, Y.; Adachi, K. *J. Magn. Magn. Mat.* **1986**, 54–57, 1267.

(49) Fujiki, S.; Shutoh, K.; Inawashiro, S.; Abe, Y.; Katsura, S. *J. Phys. Soc. Jpn.* **1986**, *55*, 3326.

(50) McCusker, J. K.; Schmitt, E. A.; Hendrickson, D. N. In *Magnetic Molecular Materials*; Gatteschi, D., Kahn, O., Miller, J. S., Palacio, F., Eds.; Kluwer Academic Publishers: 1991; pp 297–319.

(51) (a) Harvey, D. F.; Christmas, C. A.; McCusker, J. K.; Hagen, P. M.; Chadha, R. K.; Hendrickson, D. N. *Angew. Chem., Int. Ed. Engl.* **1991**, *30*, 598–600. (b) McCusker, J. K.; Christmas, C. A.; Hagen, P. M.; Chadha, R. K.; Harvey, D. F.; Hendrickson, D. N. *J. Am. Chem. Soc.* **1991**, *113*, 6114–6124.

(52) Hagen, K. S.; Westmoreland, T. D.; Scott, M. J.; Armstrong, W. H. *J. Am. Chem. Soc.* **1989**, *111*, 1907.

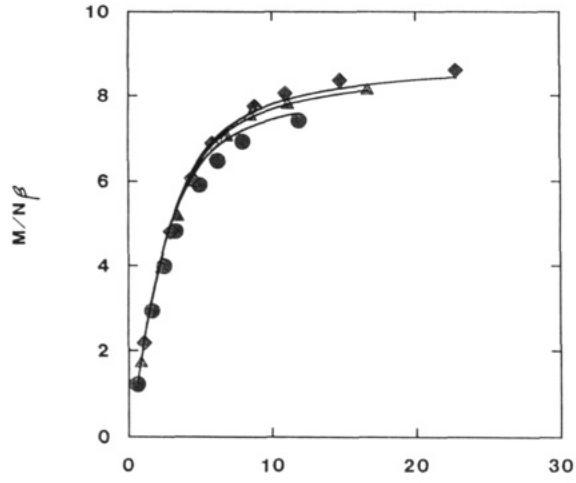

Figure 8. Plot of the reduced magnetization, $M/N\beta$, versus H/T for $[Mn_4O_3Cl_4(O_2CCH_3)_3(py)_3]\cdot{}^3/_2CH_3CN$ (**2**). The solid lines represent a calculated best fit employing a matrix diagonalization approach. Data were collected at three magnetic fields: ◇, 44 kG; △, 34.5 kG; and ○, 24.8 kG.

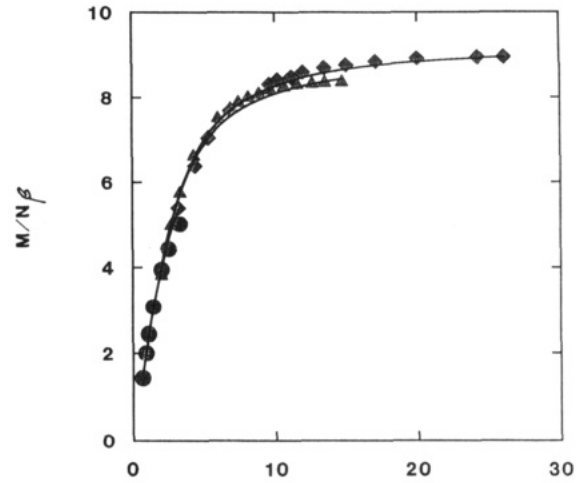

Figure 9. Plot of the reduced magnetization, $M/N\beta$, versus H/T for $[Mn_4O_3Cl_4(O_2CCH_2CH_3)_3(py)_3]\cdot{}^5/_2CH_3CN$ (**4**). The solid lines represent calculated best fit employing a matrix diagonalization approach. Data were collected at three magnetic fields: ◇, 48.0 kG; △, 30.0 kG; and ○, 10.0 kG.

the Mn^{III} ions is not directed along the μ_2-O^{2-} bridge in either of these complexes, nor is it along the μ_3-O^{2-} bridge in the cubane complexes. In short, the ferromagnetic J_{33} interaction in complexes **1**, **2**, and **4** is perhaps a reflection of the relatively acute

$$Mn^{III}\!-\!O\!-\!Mn^{III}$$

angle in these complexes, or the ferromagnetic nature of these interactions, in part, reflects the spin frustration from the $Mn^{IV}\cdots Mn^{III}$ interactions.

Magnetochemistry: Magnetization Versus Magnetic Field Studies. The above analysis of 10.0 kG susceptibility data for complexes **1**, **2**, and **4** which employs the eigenvalues from eq 8 and the van Vleck susceptibility expression, does not account for Zeeman interactions at low temperatures ($T < \sim 20$ K) or for the effects of zero-field splitting. A full-matrix diagonalization approach is needed. Furthermore, it was decided that the magnetic field dependence of the magnetization should be examined for complexes **2** and **4**. Magnetization data were collected for complex **2** at 24.8 (2.08–40 K), 34.5 (2.07–40.1 K), and 44.0 kG (1.93–39.6 K) and for complex **4** at 10.0 (3.02–14.9 K), 30.0 (2.04–15.0 K), and 48.0 kG (1.84–15.0 K). Plots of reduced magnetization, $M/N\beta$ where N is Avogadro's number and β is the nuclear Bohr magneton, versus H/T are shown in Figure 8 for complex **2** and in Figure 9 for complex **4**. Two observations can be made from these figures. For both of the complexes at the lowest temperature and highest field $M/N\beta$ saturates at a value less than 9; for complex **2** the saturation is at 8.60 and for complex **4** it is 8.96. The second observation is that for each of these complexes the three isofield data sets do *not* superimpose. If these complexes had a well-isolated $S = {}^9/_2$ ground state which was the only state populated at these temperatures, then at low temperatures and high fields $M/N\beta$ should saturate at 9.00 and the isofield data sets should superimpose. The observed dependencies of $M/N\beta$ versus H/T may be explicable in terms of an isolated $S = {}^9/_2$ ground state which is zero-field split.

Since the above fitting of variable-temperature 10.0 kG susceptibility data indicated a well-isolated $S = {}^9/_2$ ground state, the full-matrix diagonalization fitting of the variable field magnetization data employed the 10 spin functions of the $S = {}^9/_2$ state and the spin Hamiltonian of eq 11. Because the g-tensor is not expected to be very anisotropic and because there are too many

$$\hat{\mathcal{H}} = \beta_e[g_\parallel \hat{H}_z\hat{S}_z + g_\perp(\hat{H}_x\hat{S}_x + \hat{H}_y\hat{S}_y)] + D\hat{S}_{z^2} \qquad (11)$$

parameters, it was decided to assume $g_\parallel = g_\perp = g$. Only axial zero-field splitting $D\hat{S}_{z^2}$ of the $S = {}^9/_2$ state needs to be considered because the crystal site symmetry of complexes **2** and **4** is C_3. Thus, for each setting of the parameters g and D two 10×10 spin Hamiltonian matrices are constructed and diagonalized. The resulting eigenvalues, E_i, and their magnetic field dependencies, $\delta E_i/\delta H$, were used to calculate the magnetization with eq 12:

$$M = N\sum_i(-\delta E_i/\delta H)\exp(-E_i/kT)/\sum_i \exp(-E_i/kT) \qquad (12)$$

This equation reduces to the Brillouin function in the case of no zero-field splitting. If there is zero-field splitting, the calculated magnetization becomes anisotropic. The average magnetization was calculated as $M = (M_\parallel + 2M_\perp)/3$.

The $M/N\beta$ data shown in Figure 8 for complex **2** were fit by the above matrix diagonalization approach. The best fit was found with the parameters $g = 1.94$ and $D = +0.32$ cm^{-1}. The three solid lines in Figure 8 show that these parameters fit the data reasonably well. An even better fit of the data for complex **4** was obtained with $g = 2.03$ and $D = +0.28$ cm^{-1} (Figure 9). A plot of the energies versus field of the M_S components of the $S_T = {}^9/_2$ ground state for complex **4** is shown in Figure 10. It can be seen that the effect of the $D = +0.28$ cm^{-1} zero-field splitting is to split the $S_T = {}^9/_2$ state into its five Kramers doublets, with the $M_S = \pm{}^1/_2$ Kramers doublet at the lowest energy at zero field. With the magnetic field oriented in a perpendicular direction there is a mixing of the five Kramers doublets. Furthermore, when the magnetic field is increased above ~ 25 kG, the $M_S = {}^9/_2$ component becomes the ground state. Consequently, for magnetization data collected at high magnetic field and at low enough temperature so that all of the complexes populate this $M_S = {}^9/_2$ component, then there a "saturation" of magnetization and $M/N\beta$ approaches 9.0.

Two additional comments need to be made. First, the decrease in μ_{eff} observed at the lowest temperatures for complexes **1**, **2**, and **4** (Figure 3) is in part attributable to zero-field splitting. Second, fitting bulk susceptibility data does not generally provide the best evaluation of the magnitude of zero-field splittings. EPR or inelastic neutron scattering experiments can provide much better evaluations. In fact, in examining the full g, D parameter space for fitting the data for complexes **2** and **4**, one other local minimum in the least-squares error surface for the data for each complex could be found. This second fit for each complex has a negative D value with an absolute value comparable to those given above. Since D is positive for Mn^{III} single ions, the positive D values given above as fitting parameters are probably more physically reasonable. That is, the single-ion zero-field interactions at the three Mn^{III} ions and one Mn^{IV} ion vectorially project onto the $S_T = {}^9/_2$ ground state.

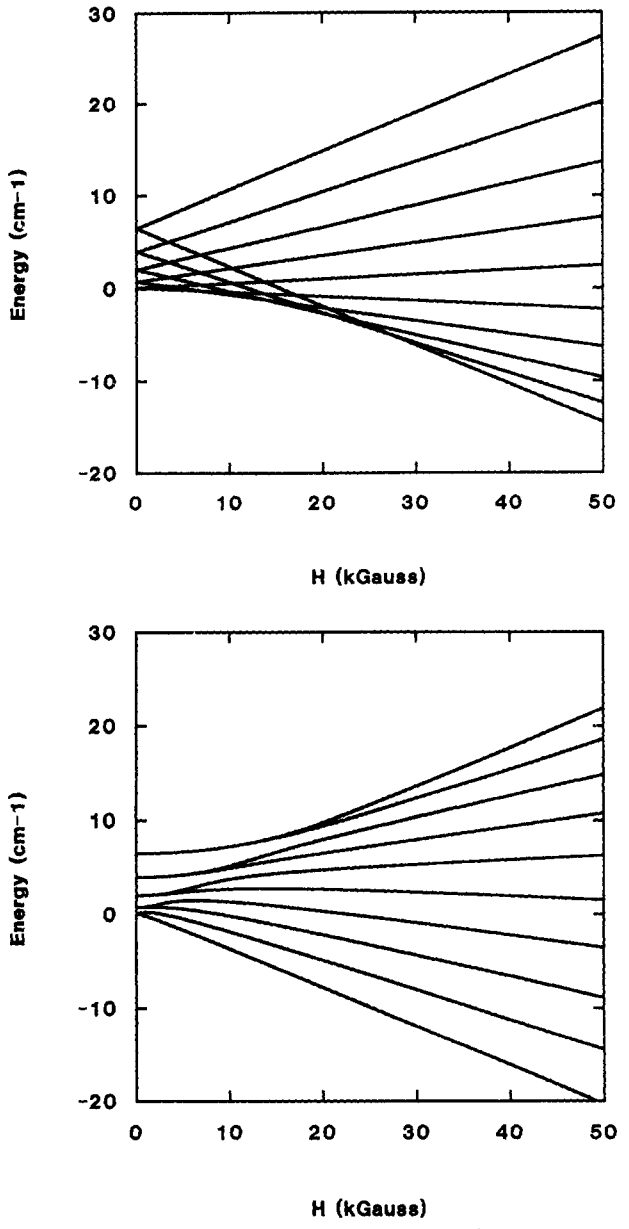

Figure 10. Plots of the Zeeman splitting of the components of the $S_T = {}^9/_2$ ground state, where for the top diagram the field is directed along the z-axis and for the bottom diagram perpendicular to the z-axis. These plots were calculated for $D = +0.28$ cm^{-1} which was evaluated for $[Mn_4O_3Cl_4(O_2CCH_2CH_3)_3(py)_3]\cdot{}^5/_2CH_3CN$ (**4**).

It is important to note that it is not possible to get fits with reasonable parameters of the the variable field magnetization data (Figures 8 and 9) for complexes **2** and **4** if it assumed that the ground state has either $S_T = {}^7/_2$ or $S_T = {}^{11}/_2$. In these cases unreasonable g values which are either >2.4 or <1.6, respectively, were obtained. Thus, regardless of the inaccuracies of determining a value of D, the magnetization data do establish that complexes **2** and **4** have $S_T = {}^9/_2$ ground states.

Finally, as noted in the previous section, it is possible that some part of the decrease in μ_{eff} observed at low temperatures (Figure 3) is due to *inter*molecular magnetic exchange interactions. In fact, the $Mn^{IV}Mn_3^{III}$ anions and H_2Im^+ imidazolium cations in complex **1** are involved in a three-dimensional hydrogen-bonding network. Since the H_2Im^+ cations are disordered in the structure, it is not easy to describe the intermolecular interactions. From a figure available in the supplementary material it is clear that there are cation–anion (H···Cl–Mn) contacts which are as short as 2.42 Å. In the case of complexes **2** and **4**, there are dimeric associations of two $Mn^{IV}Mn_3^{III}$ complexes. (A stereoview of this dimeric association for complex **4** is available in the supplementary material.) Two complexes are positioned face-to-face with the μ_3-Cl faces pointed at each other. For complex **2** the (μ_3-Cl)···(μ_3-Cl) intermolecular contact distance is 3.74 Å, whereas the same distance is 3.86 Å for complex **4**. These intermolecular contacts may qualitatively explain some of the trends in decrease of μ_{eff} seen at low temperature (Figure 3). Complex **1** with its hydrogen-bonding network exhibits the greatest decrease in μ_{eff}. The dropoff in μ_{eff} seen for complex **4** is less than that for complex **2**. The variable-temperature 10 kG susceptibility data, including the lowest temperature data, were refit where the van Vleck equation was changed to include a Weiss constant θ, i.e., T was changed to $T - \theta$. This gave four parameters: g, J_{33}, J_{34}, and θ. Figures showing the resulting least-squares fits are available in the supplementary material. For complex **1**, for example, the fitting parameters were found to be $g = 1.96$, $J_{33} = +9.31$ cm^{-1}, $J_{34} = -28.5$ cm^{-1}, and $\theta = -0.11°$. Three conclusions can be made. First, the addition of a small negative θ value does help to fit the dropoff in μ_{eff}. Second, the values of J_{33} and J_{34} are not significantly changed. Third, it will take additional experiments and more detailed theoretical work to ascertain the relative importance of zero-field, Zeeman, and intermolecular exchange interactions.

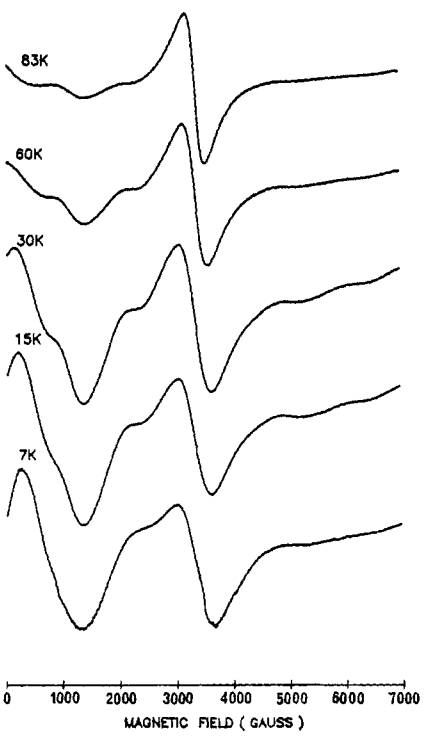

Figure 11. Temperature dependence of the X-band EPR spectrum of a polycrystalline sample of $[Mn_4O_3Cl_4(O_2CCH_2CH_3)_3(py)_3]\cdot{}^5/_2CH_3CN$ (**4**).

Electron Paramagnetic Resonance Studies. Considerable EPR data were collected for complexes **1**, **2**, and **4** as polycrystalline and frozen glass samples. At the outset, however, it must be acknowledged that the EPR spectroscopy of a $S_T = {}^9/_2$ molecule is quite complicated, and we do not purport to present a definitive analysis of all data. In Figure 11 are illustrated the X-band EPR spectra for a polycrystalline sample of the propionate complex **4**. There are low field signals which seem to lose some intensity with an increase in temperature. In the 30 K spectrum the "derivative-like" signal at 3300 G corresponds to $g = 2.03$. In this same spectrum there is a low field "bump" at ~200 G ($g \simeq 35$) as well as inflections at $g \simeq 3.1$. An expansion of the higher field portion (available in supplementary material) of this spectrum shows bumps at g values of 1.4, 1.1, and 0.95. The X-band spectra of polycrystalline samples of cubanes **1** and **2** show less features (see supplementary material). For **1** there is a broad $g \simeq 2.0$ signal and a weaker, broad signal at $g \simeq 4.0$. For **2** there is a broad $g \simeq 2.0$ signal and a weak broad bump at ~500 G ($g \simeq 12$). The Q-band (~35 GHz) spectra of polycrystalline samples of cubanes **2** and **4** were also run at 96 K (lower temperatures

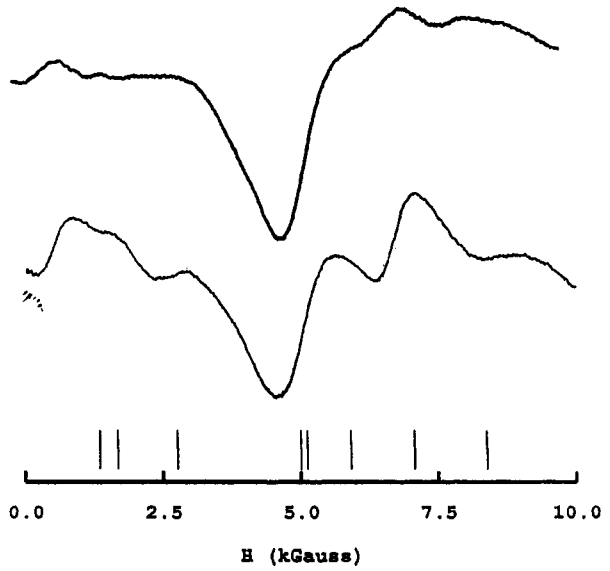

Figure 12. Low field portion of the Q-band EPR spectra of 96 K polycrystalline samples of (top) $[Mn_4O_3Cl_4(O_2CCH_3)_3(py)_3]\cdot{}^3/_2CH_3CN$ (**2**) and (bottom) $[Mn_4O_3Cl_4(O_2CCH_2CH_3)_3(py)_3]\cdot{}^5/_2CH_3CN$ (**4**). The vertical lines represent calculated resonance fields for a $S_T = {}^9/_2$ state with $D = +0.3$ cm^{-1}.

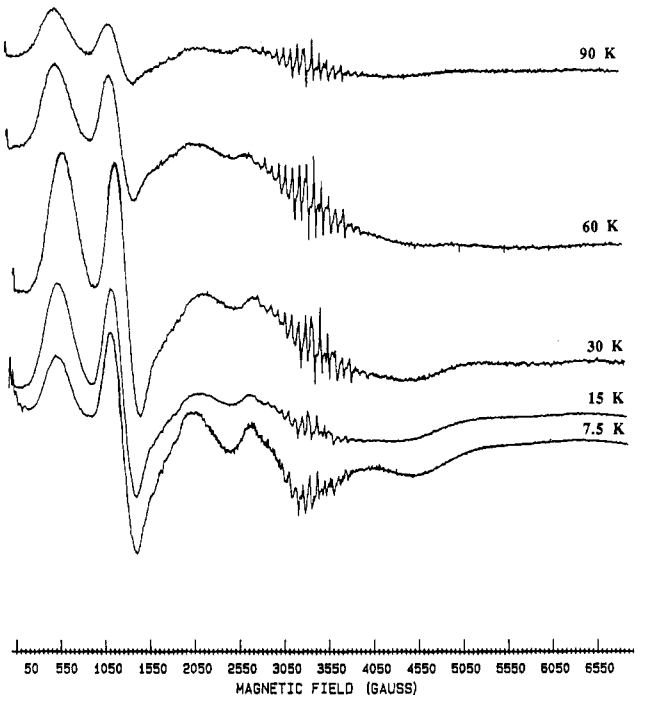

Figure 13. Temperature dependence of the X-band EPR spectrum of a 1:1 DMF/toluene glass of $(H_2Im)_2[Mn_4O_3Cl_6(O_2CCH_3)_3(HIm)]\cdot{}^3/_2CH_3CN$ (**1**).

were not available). The low field portions of these two spectra are shown in Figure 12. In both cases a derivative signal was also seen at 12400 G ($g = 2.01$).

Unfortunately these cubane complexes exhibit limited solubility in most solvents. The imidazolium salt cubane **1** shows some solubility in DMF and as indicated above obeys Beer's law in this solvent. This complex was dissolved in a 1:1 DMF/toluene mixture to employ a reasonable glassing solvent. X-band EPR spectra were run at several temperatures in the 7.5–90 K range, as shown in Figure 13. There are two low-field features at ~500 (bump, $g \simeq 12$) and ~1250 G (deriative, $g \simeq 5.2$) and a manganese hyperfine-structured $g \simeq 2.0$ signal. Broad features can be seen in the 7.5 K spectrum on both sides of the $g \simeq 2.0$ signal. It is interesting that the intensity and resolution of the hyperfine-

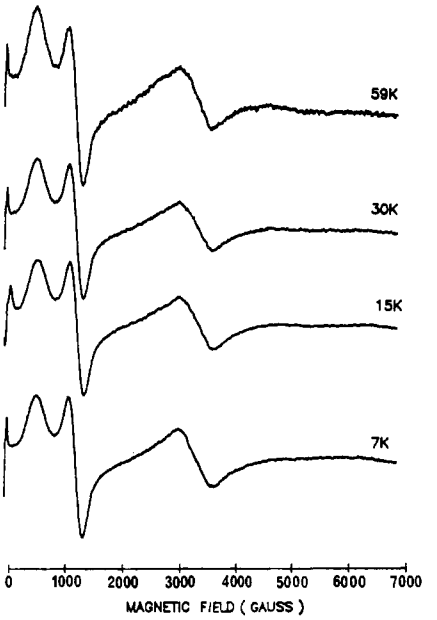

Figure 14. Temperature dependence of the X-band EPR spectrum of a 1:1 CH_2Cl_2/toluene glass of $[Mn_4O_3Cl_4(O_2CCH_2CH_3)_3(py)_3]\cdot{}^5/_2CH_3CN$ (**4**).

structured $g \simeq 2.0$ signal are maximized at ~60 K, the temperature at which μ_{eff}/molecule undergoes a maximum for the polycrystalline sample. In our communication[24] on complex **1** it was stated that the $g \simeq 2.0$ signal is due to complexes in a $S = {}^1/_2$ state. If this signal arises from the intact anion in complex **1**, then there are not $S = {}^1/_2$ complexes present. It is clear that the EPR spectra of polycrystalline examples of complexes **1**, **2**, and **4** do show relatively strong $g \simeq 2$ signals. The DMF/toluene glass spectrum of complex **1** is reproducibly obtained. However, there is some variation in line intensities in the hyperfine structure from one glass sample to another. Examination of an expanded plot (supplementary material) of this hyperfine pattern shows that there are 16–19 features at 60 K with an apparent interline spacing of ~80 G.

Since the NMR studies showed that the propionate complex **4** stays intact as an uncharged Mn_4O_3Cl complex in CD_2Cl_2, X-band EPR spectra were run for a 1:1 CH_2Cl_2/toluene glass sample. These spectra are shown in Figure 14, where it can be seen that features are clearly seen at ~500 G ($g \simeq 12$), ~1250 G ($g \simeq 5.2$), and ~3300 G ($g \simeq 2.0$). Comparison of the frozen-glass X-band EPR spectra for complexes **1** (Figure 13) and **4** (Figure 14) shows that these same three features are present in the spectra for both complexes. Frozen-glass spectra for complex **2** also show a dominance of these same features.

In addition to the cubane complexes reported in this paper five other complexes have been reported to have $S = {}^9/_2$ ground states. The X-band EPR spectra for two different $Cu^{II}Gd^{III}Cu^{II}$ complexes were reported to exhibit several features dominated by a $g = 2$ signal and to be too complicated to interpret.[53] EPR data have also been reported for a $Cu^{II}Mn^{II}Cu^{II}$ complex with an $S = {}^9/_2$ ground state.[54] The spectrum of this complex is also dominated by an intense feature at $g = 1.99$; however, weaker signals were observed at $g = 3.96$, 5.88, and 8.87. No detailed assignment was given. The complex $[L_2Fe_2(\mu\text{-OH})](ClO_4)_2$ has recently been thoroughly characterized as having an electronically delocalized Fe_2(II, III) structure with a $S = {}^9/_2$ ground state.[55] A perpendicular signal was seen at $g_\perp = 10.2$ with a weaker parallel signal at $g_\parallel = 2.3$. Both of these signals arise from the $\pm{}^1/_2$ Kramers doublet of the $S = {}^9/_2$ ground state. For this

(53) Bencini, A.; Benelli, C.; Caneshi, A.; Dei, A.; Gatteschi, D. *Inorg. Chem.* **1986**, *25*, 572.
(54) Pei, Y.; Journaux, Y.; Kahn, O. *Inorg. Chem.* **1988**, *27*, 399.
(55) Ding, X.-Q.; Bominaar, E. L.; Bill, E.; Winkler, H.; Trautwein, A. X.; Drüke, S.; Chaudhuri, P.; Wieghardt, K. *J. Chem. Phys.* **1990**, *92*, 178.

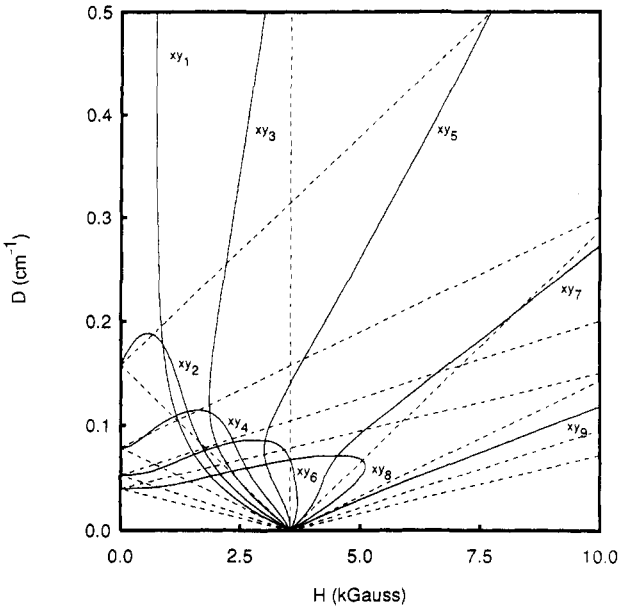

Figure 15. Calculated X-band EPR resonance fields, H(kG), as a function of the axial zero-field splitting parameter D (cm^{-1}). The solid lines are for perpendicular transitions and are labeled xy_1, xy_2, ..., xy_9 as per the convention of Weltner. The dashed lines indicate where transitions may be found with the magnetic field oriented in a parallel direction.

complex the axial zero-field splitting ($D\hat{S}_z^2$) greatly exceeds the microwave energy (~0.3 cm^{-1}) for $g = 2$ at X-band frequencies.

Finally, the preparation and characterization of $[Mn_2(biphen)_2(biphenH)(bpy)_2]$, where biphenH is 2,2'-biphenol, was very recently reported.[56] This is the first $Mn^{II}Mn^{III}$ complex which has an $S = {}^9/_2$ ground state. X-band EPR spectra for polycrystalline and frozen glass samples exhibit two main features at $g \simeq 2$ and $g \simeq 5$.

For cubane complexes **1**, **2**, and **4** the variable-field magnetization data show that D is on the order of the X-band microwave energy. In order to interpret the observed EPR spectra for these complexes it was necessary to calculate the D-dependency of the resonance fields of the allowed $\Delta M_S = \pm 1$ transitions for a complex with a $S = {}^9/_2$ ground state. We decided to generate a resonance field diagram following the general approach described by Weltner.[57] It was assumed that there is a well-isolated $S = {}^9/_2$ ground state experiencing only axial zero-field splitting ($D\hat{S}_z^2$). The magnitude of the parameter D determines the number of allowed ($\Delta M_S = \pm 1$) transitions. For each value of D, two 10 × 10 matrices were set up, one for the magnetic field parallel to the molecular z-axis and the other for the external field perpendicular to the z-axis. The resonance fields were calculated by computing the energies of the M_S components over a grid of finely spaced values of D and H. The allowed X-band EPR transitions were calculated for a frequency of $\nu = 9.43$ GHz. The positions of these $\Delta M_S = \pm 1$ allowed transitions (so-called "resonance fields") are plotted in Figure 15 as a function of the parameter D. The solid lines labeled xy_1, xy_2, ..., xy_9 correspond to perpendicular transitions within and between the five Kramers doublets comprising the $S_T = {}^9/_2$ ground state. The dashed lines represent resonance field values for the field in the parallel orientation. The perpendicular transitions are expected to dominate the observed spectrum. When D is large relative to the X-band microwave energy, only the transitions occurring within the $\pm {}^1/_2$ Kramers doublet are seen with $g_\perp \simeq 10$ and $g_\parallel \simeq 2$. The solid line xy_1 corresponds to this $g_\perp$ signal at large values of D. The xy_i transitions are labeled according to the conventions of Weltner. The xy_3, xy_5, xy_7, and xy_9 lines correspond to perpendicular transitions within the $\pm {}^3/_2$, $\pm {}^5/_2$, $\pm {}^7/_2$, or $\pm {}^9/_2$ Kramers doublets, respectively, when D is large relative to $h\nu$. At smaller values of D, the various doublets are mixed together by the magnetic field. The xy_2, xy_4, xy_6, and xy_8 lines correspond to perpendicular transitions between the Kramers doublets.

Table VII. Range of X-band EPR Resonance Fields for $[Mn_4O_3Cl_4(CH_3CO_2)_3(py)_3]\cdot{}^3/_2CH_3CN$[a] (**2**) and $[Mn_4O_3Cl_4(CH_3CH_2CO_2)_3(py)_3]\cdot{}^5/_2CH_3CN$[b] (**4**)

transition	complex **2** resonance field (G)	complex **4** resonance field (G)
xy_1	728–760	703–752
xy_3	2203–2527	1981–2293
xy_5	5012–6154	4339–5451
xy_7		8273–9540

[a] The range of axial zero-field parameter was taken as D = 0.27–0.37 cm^{-1}. [b] The range of axial zero-field parameter was taken as D = 0.23–0.33 cm^{-1}.

By fitting the variable-field magnetization data for complex **2** a D value of +0.32 cm^{-1} was obtained; for complex **4** a value $D = +0.28$ cm^{-1} was found. The range of perpendicular X-band EPR resonance fields was calculated for complex **2** by taking a range of D values of $D = +0.32 \pm 0.05$ cm^{-1}. In Table VII are given the ranges for perpendicular xy_1, xy_3, xy_5, and xy_7 transitions which are expected for a +0.27 to +0.37 cm^{-1} range of D. In a similar fashion, ranges for these same transitions were calculated for complex **4** where the range of D was taken at +0.23 to +0.33 cm^{-1}. The logic behind using a range of D values for each complex is clear. The observed peaks are broad. This is very likely due to the fact that in any environment such as a polycrystalline solid or frozen glass there will be a distribution of zero-field splittings.

As can be seen in Table VII, for complex **4** the range of xy_1 X-band resonance fields was calculated to be 703–752 G and that for the xy_3 resonance fields 1981–2293 G. Examination of the X-band EPR spectrum shown in Figure 11 for a polycrystalline sample of complex **4** shows that there are at least two low field transitions. In the 15 K spectrum, for example, there is an inflection of ~700 G, as well as a "bump" at ~2200 G. These two features may well correspond to the xy_1 and xy_3 transitions. For complex **4** the range of xy_5 resonance fields is predicted to be in the 4339–5451 G range. As mentioned above there is a bump seen at ~4950 G ($g \simeq 1.4$) in the X-band spectrum for the polycrystalline sample. However, there are also bumps seen at ~6050 G ($g \simeq 1.1$) and ~7100 G ($g \simeq 0.95$). It is possible these latter transitions are due to perpendicular transitions between components of two different Kramers doublets. The X-band CH_2Cl_2/toluene glass spectra for complex **4** shows two reasonably well-resolved low field signals at ~500 and ~1250 G (Figure 14). It appears that D is smaller for complex **4** in this glass medium than in the crystal environment. Perhaps these two peaks correspond to the xy_1 and xy_2 transitions; however, it is not clear then where the xy_3 transition is. It is clear that complex **1** in a DMF/toluene glass (Figure 13) also shows the same two low field transitions.

The Q-band spectra for polycrystalline samples of complexes **2** and **4** (Figure 12) provide a further check on our evaluation of the zero-field splitting. The resonance fields were calculated for $D = 0.30$ cm^{-1} with a microwave frequency of 34.9 GHz. The positions of these calculated transitions are shown as vertical lines below the experimental spectra in Figure 12. As can be seen, there is reasonable agreement between the features seen in these two spectra and the resonance fields calculated for $D = 0.30$ cm^{-1}.

More effort is needed to understand fully the EPR signals from these $Mn^{IV}Mn_3^{III}O_3Cl$ cubane complexes. The presence of low field fine structure in the X-band spectra of the complexes indicates that the zero-field splitting parameter is of the order of the X-band microwave energy, 0.3 cm^{-1}. The $g \simeq 2$ signal seen both at X- and Q-band frequencies has not been fully explained. It is tempting to associate this signal with some binuclear $Mn^{IV}Mn^{III}$ $S = {}^1/_2$ complex which results from a small decomposition of the cubane complex. However, the relative intensity of this $g \simeq 2$ signal is very similar for cubane **1** in a DMF/toluene glass or

(56) Schake, A. R.; Schmitt, E. A.; Conti, A. J.; Streib, W. E.; Huffman, J. C.; Hendrickson, D. N.; Christou, G. *Inorg. Chem.* **1991**, *30*, 3192–3199.

(57) Weltner, W., Jr. *Magnetic Atoms and Molecules*; Scientific and Academic Editions: New York, 1983.

cubane **4** in a CH_2Cl_2/toluene glass. In these cases some part of these signals may be attributable to the parallel transition of the $\pm^1/_2$ Kramers doublet. In the EPR spectra for the polycrystalline samples of **1**, **2**, and **4** this $g \simeq 2$ signal is very dominating in the spectrum. It probably cannot be just due to an impurity then. In a polycrystalline sample it is possible that very weak intermolecular magnetic exchange interactions may be the origin of this $g \simeq 2$ signal. If such an intermolecular exchange interaction is present, this could lead to an exchange of electrons between cubane complexes at a frequency greater than the microwave frequency. An average $g \simeq 2$ signal would result. In fact, it is interesting that this $g \simeq 2$ signal is most intense in the spectrum for complex **1**. There is a hydrogen-bonding network involving the cations and anions in complex **1**. Compared to the spectrum for complex **2**, that for polycrystalline complex **4** shows less intensity in the $g \simeq 2$ signal. These two complexes are, of course, isostructural, and the propionate **4** has more intermolecular shielding than does the acetate **1**.

Concluding Comments. The preparation and physical characterization of four distorted cubane $Mn^{IV}Mn_3^{III}O_3Cl$ complexes have been presented. These four complexes were formed by the reaction of a μ_3-oxide–Mn_3^{III} complex with Me_3SiCl. It was shown that the $Mn^{IV}Mn_3^{III}O_3Cl$ complexes result from a disproportionation. The X-ray structures of the four complexes show that the $Mn^{IV}Mn_3^{III}O_3Cl$ core in each complex is very similar. This core is best considered as a Mn_4 pyramid with the Mn^{IV} ion at the apex, the μ_3-Cl^- ion bridging the basal plane, and a μ_3-O^{2-} ion bridging each of the three remaining faces of the Mn_3^{III} basal plane. It is described in detail how the structure of this $Mn^{IV}Mn_3^{III}O_3Cl$ cubane core is related to the butterfly cores of structurally characterized $Mn_4^{III}(\mu_3\text{-}O^{2-})_2$ and $Mn_2^{II}Mn_2^{III}(\mu_3\text{-}O^{2-})_2$ complexes. The former $Mn_4^{III}O_2$ complexes have been proposed[26] as model complexes for the S_1 state of the WOC of photosystem II.

A variety of physical data were presented to probe the electronic structure of these $Mn^{IV}Mn_3^{III}O_3Cl$ complexes to see how well they model the S_2 state of the WOC. These complexes were shown not to exhibit any reversible electrochemistry; ^1H and ^2H NMR studies showed that the cubane complexes very likely stay intact in solution. Detailed variable-temperature and variable-field studies of complexes **1**, **2**, and **4** show that these complexes have a $S_T = {}^9/_2$ ground state, which apparently results from antiferromagnetic Mn^{IV}···Mn^{III} interactions combined with ferromagnetic Mn^{III}···Mn^{III} interactions. The $S_T = {}^9/_2$ ground state is well isolated from excited states. X- and Q-band EPR studies confirm that the ground state of these complexes has a spin larger than $^1/_2$ and that it is well-isolated. The EPR spectra were shown to be consistent with a $S_T = {}^9/_2$ ground state with axial zero-field interactions of the order of $D \simeq 0.3$ cm^{-1}.

Since the S_2 state of the WOC has been reported to have either a $S_T = {}^1/_2$ or $S_T = {}^3/_2$ ground state, it is clear that the $S_T = {}^9/_2$ ground state $Mn^{IV}Mn_3^{III}O_3Cl$ complexes reported in this paper do not model the electronic structure of the S_2 state. Nevertheless, the fact these cubane complexes have a $S_T = {}^9/_2$ ground state is intrinsically interesting. It is shown that the intermediate-spin ground state results from spin frustration. The antiferromagnetic Mn^{IV}···Mn^{III} interactions dominate the Mn^{III}···Mn^{III} interactions such that the three Mn^{III} ions have their spins aligned ($S_A = 6$). The nature of other possible spin frustrated ground states is described in detail. Two $S_T = {}^1/_2$ states are candidates for the ground state if the J_{34}/J_{33} exchange parameter ratio is correct. To change the ground state of the cubane $Mn^{IV}Mn_3^{III}O_3Cl$ complexes from $S_T = {}^9/_2$ to $S_T = {}^1/_2$ it is necessary to change the Mn^{III}···Mn^{III} interaction so that it is antiferromagnetic and of more comparable magnitude to the antiferromagnetic Mn^{IV}···Mn^{III} interactions.

Acknowledgment. This work was supported by NIH Grants GM 39083 (to G.C.) and HL 13652 (to D.N.H.). We thank Michael S. Wemple for technical assistance.

Supplementary Material Available: Complete listings of atomic coordinates, isotropic and anisotropic thermal parameters, bond lengths and angles for complexes **1**, **2**, **4**, and **5**, and magnetic susceptibility data for complexes **1**, **2**, and **4** (41 pages); listings of observed and calculated structure factors for complexes **1**, **2**, **4**, and **5** (18 pages). Ordering information is given on any current masthead page.